COLLABORATIVE MOBILE TARGET IMAGING IN ULTRA-WIDEBAND WIRELESS RADAR SENSOR NETWORKS

A THESIS SUBMITTED TO
THE GRADUATE SCHOOL OF NATURAL AND APPLIED SCIENCES
OF
MIDDLE EAST TECHNICAL UNIVERSITY

BY

MUHARREM ARIK

IN PARTIAL FULFILLMENT OF THE REQUIREMENTS
FOR
THE DEGREE OF MASTER OF SCIENCE
IN
ELECTRICAL AND ELECTRONICS ENGINEERING

NOVEMBER 2008

Approval of the thesis:

COLLABORATIVE MOBILE TARGET IMAGING IN ULTRA-WIDEBAND WIRELESS RADAR SENSOR NETWORKS

submitted by **MUHARREM ARIK** in partial fulfillment of the requirements for the degree of **Master of Science in Electrical and Electronics Engineering Department, Middle East Technical University** by,

Prof. Dr. Canan Özgen _____
Dean, Graduate School of **Natural and Applied Sciences**

Prof. Dr. İsmet Erkmen _____
Head of Department, **Electrical and Electronics Engineering**

Assoc. Prof. Dr. Özgür Barış Akan
Supervisor, **Electrical and Electronics Engineering Dept., METU** _____

Examining Committee Members:

Prof. Dr. Mete Severcan _____
Electrical and Electronics Engineering Dept., METU

Assoc. Prof. Dr. Özgür Barış Akan _____
Electrical and Electronics Engineering Dept., METU

Asst. Prof. Dr. Ali Özgür Yılmaz _____
Electrical and Electronics Engineering Dept., METU

Asst. Prof. Dr. Çağatay Candan _____
Electrical and Electronics Engineering Dept., METU

Metin Aktaş (M.Sc.) _____
MGEO Division, ASELSAN Inc.

Date: _____

I thereby declare that all information in this document has been obtained and presented in accordance with academic rules and ethical conduct. I also declare that, as required by these rules and conduct, I have fully cited and referenced all material and results that are not original to this work.

Name, Last name : Muharrem ARIK

Signature :

ABSTRACT

COLLABORATIVE MOBILE TARGET IMAGING IN ULTRA-WIDEBAND WIRELESS RADAR SENSOR NETWORKS

Arık, Muharrem

M.Sc., Department of Electrical and Electronics Engineering

Supervisor: Assoc. Prof. Dr. Özgür Barış Akan

November 2008, 68 pages

Wireless sensor networks (WSN) have thus far been used for detection and tracking of static and mobile targets for surveillance and security applications. However, detection and tracking do not suffice for a complete satisfaction of these applications and an accurate target classification. To address this need, among various target classification methods, imaging of target yields the most valuable information. Nevertheless, imaging of mobile targets moving over an area requires networked and collaborative detection, tracking and imaging capabilities. With this regard, ultra-wideband (UWB) radar technology stands as a promising approach for networked target imaging over an area due to its unique features such as having no line-of-sight (LoS). However, the UWB wireless radar sensor network (WRSN) is yet to be developed for high quality imaging of mobile targets.

In this thesis, an architecture for UWB wireless radar sensor network and a new collaborative mobile target imaging (CMTI) algorithm for UWB wireless radar sensor networks (WRSN) are presented. It is intended to accurately and efficiently

obtain an image of mobile targets based on the collaborative effort of deployed UWB wireless radar sensor nodes. CMTI enables detection, tracking and imaging of mobile targets with a complete WRSN solution. CMTI exploits mobility of the target in the sensor field to build its own multi-static radar aperture. Performance evaluations reveal that CMTI obtains high quality radar image of mobile targets in WRSN with very low communication overhead and energy expenditure.

Keywords: Mobile Target Imaging, CMTI, UWB Wireless Radar Sensor Networks, Collaborative Radar Imaging.

ÖZ

ÇOK GENİŞ BANT KABLOSUZ RADAR SENSOR AĞLARINDA HAREKETLİ HEDEFLERİN İŞBİRLİKÇİ GÖRÜNTÜLENMESİ

Arık, Muharrem

Yüksek Lisans, Elektrik ve Elektronik Mühendisliği Bölümü

Tez Yöneticisi: Doç. Dr. Özgür Barış Akan

Kasım 2008, 68 sayfa

Gizlice izleme ve güvenlik uygulamalarında, statik ve mobil hedeflerin tespit ve takip edilmesi için şimdiye kadar kablosuz algılayıcı ağları kullanıldı. Ancak, bu uygulamaların tam başarısı ve hedefin doğru sınıflandırılması için, hedefin sadece tespit ve takibi yetersiz kalmaktadır. Bu ihtiyaç karşısında, çeşitli hedef sınıflandırma yöntemleri arasında, hedefin görüntülenmesi en değerli bilgiyi vermektedir. Bununla birlikte, bir alandan geçip giden hareketli hedeflerin görüntülenmesi, işbirlikçi ve ağ yapısında tespit, takip ve görüntüleme kabiliyetlerini gerektirir. Bu durumda, görüş çizgisi gereği olmaması gibi benzersiz özellikleri nedeniyle, çok geniş bant radar teknolojisi, alandan ağ yapısında hedef görüntüleme için umut verici bir yaklaşım olarak durmaktadır. Fakat, hareketli hedeflerin yüksek kalitede görüntülenmesi sağlayabilecek çok geniş bant kablosuz radar sensor ağları henüz geliştirilmemiştir.

Bu tezde, çok geniş bant kablosuz radar algılayıcı ağ mimarisi ve yeni bir işbiklikçi hareketli hedef görüntüleme (İHHG) algoritması çok geniş bant kablosuz radar sensor ağları için sunuldu. Bu algoritmada, sahaya yerleştirilmiş çok

geniş bant radar algılayıcı düğümlerinin işbirlikçi çabalarıyla hareketli hedeflerin görüntüsünün, doğru ve etkin bir şekilde elde edilmesi amaçlanmıştır. İHHG, tam bir kablosuz radar sensor ağı çözümüyle hareketli hedeflerin tespit ve takip edilmesini ve görüntülenmesini sağlar. İHHG, kendi çoklu radar açıklığını oluşturmak için algılayıcı alanı içerisindeki hedefin hareketinden faydalanır. Başarım değerlendirmeleri, İHHG algoritmasının, çok düşük iletişim yükü ve enerji harcaması ile kablosuz radar algılayıcı ağı içerisinde, hareketli hedeflerin yüksek kalitede radar görüntüsü elde edebildiğini göstermiştir.

Anahtar Kelimeler: Mobil Hedef Görüntüleme, İHHG, Çok Geniş Bant Kablosuz Radar Sensör Ağları, İşbirlikçi Radar Görüntüleme.

To my family, and
To my Angel

ACKNOWLEDGMENTS

I would like to express my gratefulness and deepest respect to my advisor, Dr. Özgür B. Akan. I am indebted to Dr. Akan for his constant support during my graduate study. This thesis would not be completed without his mentorship and trust.

I also thank Dr. Mete Severcan, Dr. A. Özgür Yılmaz, Dr. Çağatay Candan and M.Sc. Metin Aktaş who kindly agreed to serve in my M.Sc. Examining Committee.

I also would like to thank all the members of the Next generation Wireless Communications Laboratory (NWCL) for their support during my graduate study.

I am indebted to all of my friends and colleagues for their support and encouragements. I am also grateful to ASELSAN Inc. for the facilities that made my work easier.

Finally, I am so grateful to my family, Sabire and Ali Arık, for their love, support and encouragement, and I thank my brilliant Angel, who supported me during my seemingly endless working hours even at the very first days of our relationship.

TABLE OF CONTENTS

LIST OF TABLES

LIST OF FIGURES

LIST OF SYMBOLS

2D	Two Dimensional
CMTI	Collaborative Mobile Target Imaging
SBP	Standard Back-Projection
CBP	Cross Correlated Back-Projection
SRRS	Smallest Range Resolution Selection
WSN	Wireless Sensor Network
WRSN	Wireless Radar Sensor Network
UWB	Ultra-Wideband
ISAR	Inverse Synthetic Aperture Radar
LOS	Line Of Sight
RF	Radio Frequency
SNR	Signal to Noise Ratio
TDoA	Time Difference of Arrival
ToF	Time of Flight

CHAPTER 1

INTRODUCTION

Ultra-Wideband Wireless Radar Sensor Network is emerging as enabling technology for border surveillance in homeland security, as intrusion monitoring, unauthorized movement of targets around critical infrastructure and facilities.

In Wireless Sensor Network (WSN) systems, low power UWB radars are recently used [16]. Generally, UWB radar sensors are used in detection, tracking and localization of the intruder in the sensor field [13], [14], [15], [22]. However, detection and tracking do not suffice for a complete satisfaction of an accurate target classification in surveillance applications.

In order to accomplish this need, radar sensor trace based techniques have been used for classification of the intruder [15]. Signal traces of walking and running person, driving vehicle is presented. However, these techniques may not be sufficient to determine the shape and features of the mobile target.

Moving target 2D UWB radar is introduced in [21], with two receiving antennas using modification of time-domain back-projection technique. It is just a UWB radar demonstration using real-time sampling in laboratory environment, there is no multi-static radar or sensor network structure used for imaging. However, in this work a moving target filter is used for target imaging as we suggested.

Object detection and imaging via sensor network structure is presented in a recent work [13], with multi-static imaging of fixed objects or invariant environment. In [13], radar sensor nodes are divided into two groups, anchors and observers, in

the WSN structure. However, imaging process is applied only for the static environments by using mobile radar sensors. In this work, in order to obtain high quality radar image, large number of samples of the object need to be taken and transported to a specific location, i.e., the sink, which would incur huge amount of traffic, and hence, potentially lead to congestion in the network. However, radar image quality and communication challenges are not mentioned and not investigated in [13].

Imaging of mobile targets moving over a field requires collaborative detection, tracking and imaging capabilities. However, these capabilities impose additional set of significant challenges such as amplified node and transceiver complexities, need for energy-efficient radar imaging algorithms for a high quality radar image.

With this regard, ultra-wideband (UWB) radar technology can be used for networked collaborative target imaging over a field due to its unique features. UWB radar sensors can provide detection, localization and imaging of targets in short range regardless of environmental conditions [13], as they can operate in all weather conditions, including fog, rain, sleet, hail, snow, and sand. Lower frequencies in UWB spectrum provide looking into or through non-metallic materials and targets. Radar sensors maintain their accuracy in bad conditions and they can still produce good results in non line-of-sight (non-LOS) situations. Since UWB signals have extremely large bandwidth, the targets can be easily detected in the environment [7]. With these advantages, UWB systems are used for applications such as, target recognition and imaging, indoor navigation and surveillance, through wall detection, ground penetrating systems, border surveillance systems.

In the classification process, UWB radar image of the mobile target is required to accurately assess the threat level of the mobile intruder. Spatially distributed radar nodes can gather comprehensive knowledge on the mobile targets in the field. For accurate classification, decision can be made from UWB radar images formed by WRSN. Using the advantages of UWB radar systems, the feature and shape of the moving target in the sensor field can be specified from the radar image, so the classification process of the target gets easy with using the dimensions and features. However, the UWB wireless radar sensor network (WRSN) is yet to be developed

for high quality imaging of mobile targets.

In this thesis, we introduce an architecture for UWB wireless radar sensor network and a new collaborative mobile target imaging algorithm, called *CMTI*. The algorithm seeks to accurately and efficiently obtain an image of mobile targets based on the collaborative effort of deployed UWB radar sensor nodes. It uses static radar sensor nodes for tracking and imaging process and exploits movement of the target in the sensor field to build own multi-static radar synthetic aperture. Then, CMTI forms an image of the mobile target relative to the deployment of the radar sensor nodes, the target mobility behavior and also radar cross section (RCS) of the target. It uses smallest range resolution selection with threshold (SRRS-th) component of CMTI to provide higher quality in radar images. CMTI also adopts forward error correction (FEC) schemes to provide reliable transport of observations to sink node over multi-hop paths. Importantly, the imaging part of CMTI mainly run on the sink and CMTI does not require complex operations at resource constrained radar sensor nodes. It achieves high quality radar image in a communication efficient way using multi-static radar structure of the radar sensors in the WRSN.

1.1 Organization of the Thesis

The remainder of this thesis is organized as follows. In Chapter 2, Ultra-Wideband radar technology is explained. In Chapter 3, the proposed WRSN structure is introduced and the architecture of the radar sensor nodes are explained. In Chapter 4, the collaborative mobile target imaging algorithm, CMTI, is presented in detail along with its operational phases. Error analysis of CMTI is discussed in Chapter 5, where the sources of error which affect image quality are pointed out. In Chapter 6, performance evaluation is presented and the obtained results are discussed. Finally, concluding remarks are given in Chapter 7.

CHAPTER 2

ULTRA-WIDEBAND TECHNOLOGY

In this chapter, firstly, Ultra-Wideband systems and their advantages are shortly explained. Then, the usage of Ultra-Wideband techniques in radar sensor and transceiver technology which are used in Wireless Sensor Networks are mentioned.

2.1 Ultra-Wideband Systems

The UWB, generally can be defined as communication or transmission electronic systems with instantaneous spectral occupancy in excess of 500 MHz or a fractional bandwidth of more than 0.2. The bandwidth and fractional bandwidth of UWB systems can be given as,

$$Spectral\ \ Occupancy = f_H - f_L$$

$$Fractional\ \ Bandwidth = \frac{2(f_H - f_L)}{(f_H + f_L)}$$

where f_H and f_L are the higher and the lower frequencies respectively, at the -10 dB emission point. In the Federal Communications Commission (FCC) standards, the UWB frequency spectrum range is defined from 3.1 to 10.6 GHz [1]. We can see a comparison of the power spectrum of the UWB & NB systems in the Fig. 2.1.

An ultra-wideband signal can be described as a carrier-free, impulse, baseband, time-domain, nonsinusoidal signals [3]. A UWB radio systems use baseband impulses modulated in time, by amplitude or by modulating any other signal characteristic.

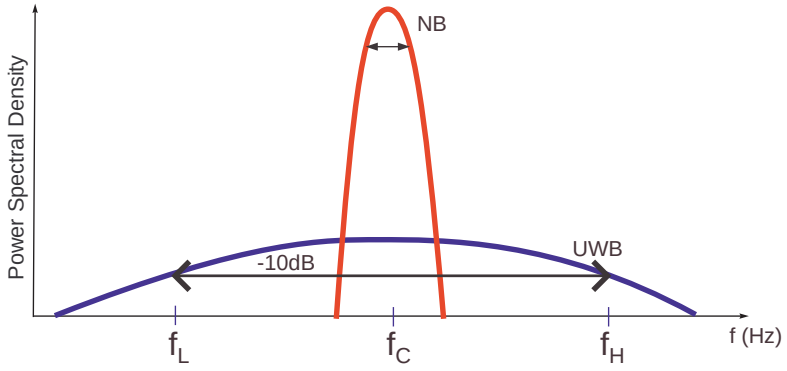

Figure 2.1: UWB and NB Systems Power Spectrums

A wider bandwidth provides better multipath and interference mitigation, improved imaging and ranging accuracy and for communication systems means more users and higher data rate. Besides, a lower center frequency for a given bandwidth provides better materials penetration e.g. through the walls and doors. UWB devices transmit millions of very low power radio impulses, each typically less than a nanosecond over a very wide radio spectrum. UWB uses the existing spectrum that is currently being used by other conventional radio communication devices. The energy of UWB signal is much below than the thermal noise of other conventional devices (e.g. GPS, Wireless LAN, Bluetooth, Cellular Phones etc).

UWB radar can identify underground objects e.g. land mines, locate persons hidden behind a wall or under debris. Besides, it can provide location of steel reinforcement bars in concrete, electrical wiring and pipes hidden in a wall. With these advantages, UWB systems are used for applications such as, target recognition and imaging, indoor navigation and surveillance, through wall detection, ground penetrating systems, border surveillance systems.

2.2 Ultra-Wideband in Wireless Sensor Networks

In WSN, Ultra-Wideband technology is recently used for building low-cost, low-power radar sensor and wireless transceiver in sensor node structure.

2.2.1 UWB Radar Sensor

UWB technology promises target recognition, identification, classification and imaging in radar applications. With UWB technology, the information from the reflected radar signals is increased as a result of the decrease in the pulse duration [4]. Then UWB can provide,

- higher range resolution, consequently higher accuracy in range and position measurements
- easier recognition of targets when forming their radar images
- improved radar immunity to passive interferences like rain, fog, clutter, chaff since the interference RCS of these short pulses are comparable with target RCS
- reduction in the radar dead zones
- increased probability of target detection
- immunity to external narrowband electromagnetic interferences and noise

Within the usage of UWB as a low-cost and low-power radar sensors in WSN, sensor nodes maintain their accuracy in bad conditions during their extended lifetime and they can still produce good results in non line-of-side (non-LOS) situations. Since UWB signals have extremely large bandwidth, the mobile targets can be easily detected in the environment [7].

2.2.2 UWB Wireless Communications

Wireless sensor networks (WSN) have been widely used in space monitoring, environment monitoring. It uses a wide range of information technology that spans hardware, systems software, networking, and programming methodology [5]. There are many wireless standards such as Bluetooth and WLAN, but they are not suitable

for low power consumption applications such as WSN. In fact, radio transceivers almost responsible for the whole power consumption of a wireless sensor node. Generally, the targeted lifetime of one node is about one to five years. With a single 1.5-V AA alkaline battery, the average power consumption must range from 100 to 10 microwatts [5]. However, today's commercially available radio transceivers consume typically several 10s of milliwatts [5].

Using UWB techniques is recognized to be a cost-effective way to be integrated in the WSN instead of traditional radio transceiver, because UWB techniques has the possibility of achieving high throughput, long range, low power consumption, position location, ranging capability and low cost [5]. IEEE 802.15.4a [2] (WPAN) formed a study group, whose goal is to deliver the standard specification for a UWB-based network of sensors or other low-power, low cost wireless devices such as RFID supporting low data rate in individual links while the access point should support high aggregated throughput [5].

For low power UWB, WPAN, which has high data rate for very short range, is in use in the United States and it is mainly dedicated to civilian needs. It is about the use of UWB in the field of domestic networks. This technology would allow to replace cables between devices, i.e., printers, screens and computers, with short range, wireless connections in the headquarter [6]. Another military application could be to use a typical wireless short range (WPAN) communication system instead of cables for the soldier radio architecture [6].

CHAPTER 3

WIRELESS RADAR SENSOR NETWORK ARCHITECTURE

In this chapter, an architecture for wireless radar sensor networks (WRSN) is introduced. WRSN is considered to be built of two layered structure, i.e., *target detection layer*, and *target imaging layer* as seen in the Fig. 3.1. Target detection layer is composed of magnetic, ultrasonic, seismic or infrared type sensor for motion detection process, and the target imaging layer has UWB radar sensors to be used for radar imaging of mobile targets. Clearly, considering the energy constraints of sensor nodes, the target imaging layer is not always active during the entire operation of WRSN. The nodes in the target detection layer are assumed to be always awake, and once the target is detected, WRSN nodes in the target imaging layer are activated.

The sensor nodes in the target detection layer have only mobile target detection feature. They are expected to communicate the area and time of detection to the sink node. In this way, sink can wake up the radar sensor nodes in the target imaging layer over the region of detection, i.e., *event field*.

In target imaging layer of WRSN, there are two type of radar sensor node, i.e., *anchor* as a UWB radar transmitter and *observer* as a UWB receiver. Observer is equipped with UWB receiver, and it has sensing capability of UWB signals from the environment. Anchor has a capability of generating coded impulses from UWB transmitter.

WRSN considered here has short range low power radar sensors to be used in surveillance applications. The radar sensor node hardware architecture must be

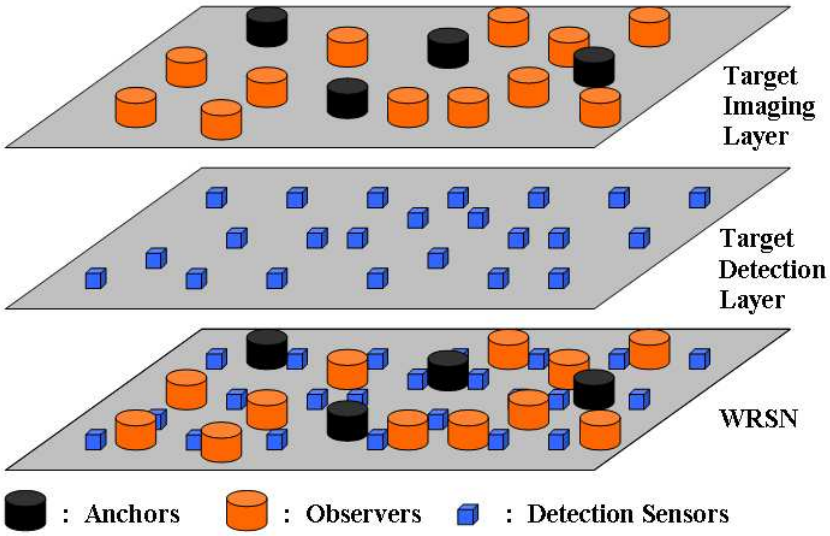

Figure 3.1: Wireless Radar Sensor Network Architecture

less complex to respond power constraints in WRSN structure. They should have a capability of specifying accurate radar range profile of the mobile target.

Operation of observer receiver hardware is based on the important principle of *range-gating*. The receiver looks for the return signals, and the analog to digital converter samples only those signals that fall in a narrow time window, called *range-gate* [16]. Hence, some part of the observation can be taken during each pulse interval with sweeping range-gate with a delay. After certain amount of time, complete set of samples of the entire signal can be obtained. The receiver of the observer is a simple correlation detection receiver which compares an interval of received signal with a reference waveform. Then, receiver outputs a value proportional to the integral of the product over that interval. Besides, correlation detection receiver can also be equivalently defined as matched filtering, that is filtering the signal with its time reversed version. Here, it is assumed that the returning pulses do not change within a time period of several pulses long. For the range measurement, observer uses time difference of arrival (TDoA) algorithm, with using time difference between direct-path arrival and multi-path arrival from target.

On the other hand, the static and time-variant clutter is one of the main problems for the radar receivers, as there exist many clutters in the environment due to large UWB receiver bandwidth. However, in this work, only time-invariant clutters are assumed to exist in the field and a basic moving target filter is proposed to avoid static clutter effect in the observer hardware architecture [21]. A basic averaging background subtraction technique is used [26], because for the simplicity of observer hardware. However, as a future work, a variety of background subtraction methods, such as adaptive averaging methods, parametric or non-parametric multimodal background models [25] can be used and their effects on the radar images can be investigated.

The anchor node hardware adopted here consists of impulse generators which generate compressed impulses in a pseudo-random manner. Impulse generator generates Gaussian impulses with anchor pulse-width (PW).

Wireless sensor network systems generally have power constraints on sensor node hardware architecture. Same as WSN, here in WRSN, one of the main factor, which affects anchor node power consumption is the anchor node radar transmitted power. In order to minimize anchor node radar transmitted power consumption, we should determine anchor node minimum transmitted power, (P_{min}^{anc}), to provide accurate detection of mobile target at maximum range for the proposed WRSN structure. To this end, firstly, minimum required power for accurate detection in the observer, P_{th}, needs to be calculated to find P_{min}^{anc}.

In order to find P_{th}, we should specify an expression for the signal to noise ratio (SNR) at the observer. Each anchor-observer pair composes a bistatic radar structure. In a bistatic radar, with narrow band (NB) pulses the received power, P_{obs}, can be evaluated by using the Friis' formula [14]. However, the formula for narrowband signals is no longer true in UWB domain since the wavelength can vary within the signal's large band. Therefore, the Friis' formula over all wavelengths should be integrated over the frequency interval $[f_L, f_U]$ [14], [27]. For the anchor-target-observer multi-path,

$$P_{obs}^{UWB} = \int_{f_L}^{f_L+B} \frac{S_{anc}(f)G_{anc}(f)G_{obs}(f)\sigma_B}{(4\pi)^3 (R_{anc}^2 R_{obs}^2)} (c/f)^2 \, df \tag{3.1}$$

where $S_{anc}(f)$ is the one-sided transmitted power spectral density, $G_{anc}(f)$, $G_{obs}(f)$ are the frequency-dependent antenna gains, and $B = f_U - f_L$ is the signal bandwidth, σ_B is the object bistatic RCS and also R_{anc} is the distance from anchor to object and R_{obs} is the distance from observer to object.

Considering a white spectrum for the transmitted signal from anchors, constant antenna gains and constant RCS over frequencies $[f_L, f_U]$, then the formula becomes [14],

$$P_{obs}^{UWB} = \frac{S_{anc}G_{anc}G_{obs}\sigma_B c^2}{(4\pi)^3 (R_{anc}^2 R_{obs}^2)} \left(\frac{1}{f_L} - \frac{1}{f_L + B} \right) \tag{3.2}$$

where S_{anc} is the transmitted power spectral density, G_{anc}, G_{obs} are the constant antenna gains, B is the signal bandwidth, c is the speed of light, σ_B is the target bistatic RCS, R_{anc} is the distance from anchor to target and R_{obs} is the distance from observer to target. Then, Signal-to-Noise Ratio (SNR) is,

$$SNR_{UWB} = \frac{N_s P_{obs}^{UWB}}{N_0 PRF} \tag{3.3}$$

where P_{obs}^{UWB}/PRF represents the received energy per scattered pulse, and N_s is the processing gain and N_0 is the noise power at the observer. For typical correlation detection in the observer receiver, we assume that the threshold SNR at maximum range is SNR_{th}. P_{th} can be expressed as,

$$P_{th} = \frac{SNR_{th} N_0 PRF}{N_s} \tag{3.4}$$

As observed in (3.3), in order to improve the received signal quality at the observer or to minimize threshold power level in (3.4), PRF used by the anchor nodes needs to be as small as possible.

Observer nodes use equivalent-time sampling method in their UWB receivers. For gathering a complete signal, $S \times RG_w$ seconds, at the receiver, where S is the total number of samples for gathering a complete observation and RG_w is the range-gate width, the receiver can take this signal in,

$$T_\sigma = S/F_{ADC} \tag{3.5}$$

seconds, F_{ADC} is the observer analog to digital converter sampling frequency. Besides, PRF for anchor must be linearly dependent to F_{ADC} at the observer as,

$$PRF = kF_{ADC} \tag{3.6}$$

where k is any positive integer. Therefore, with combining (3.5) and (3.6),

$$PRF = kS/T_\sigma \tag{3.7}$$

As said before we try to minimize PRF to minimize threshold received power P_{th} at the observer. For minimum PRF, k is selected as 1 and minimum PRF becomes S/T_σ.

However, there is a limitation on PRF, while mobile target is sensing from [17] and [18]. In mobile target scenario, a relation is detailed for devices which uses equivalent-time sampling method in [17] as,

$$4T_\sigma V_{max} < (c/B) \tag{3.8}$$

where V_{max} is the maximum mobile target radial velocity to observer, B is the total sensed frequency band, c is the speed of light. Then, we can talk about the time-invariance of the received signal [17]. If the signal is time-invariant, then it can be accepted that the total received signal with equivalent time sampling is almost the same as the real signal.

If (3.8) is modified with (3.7) when k is 1 as,

$$(4S\,V_{max})/PRF < (c/B) \tag{3.9}$$

and minimum value for PRF (PRF_{min}) becomes,

$$PRF_{min} = (4V_{max}BS)/c \tag{3.10}$$

then, for a different maximum mobile target radial velocities, PRF_{min} changes linearly.

With using PRF_{min} for a selected V_{max}, the threshold received power at the observer required for accurate detection ,P_{th}, can be expressed as,

$$P_{th} = \frac{SNR_{th}N_0PRF_{min}}{N_s} \tag{3.11}$$

then, minimum transmitted power is stated in [14] as,

$$P_{min}^{anc} = \frac{P_{th}(R_{anc}R_{obs})_{max}^2(4\pi)^3}{G_{anc}G_{obs}\sigma_B[\frac{1}{f_L} - \frac{1}{f_L+B}]c^2}B \tag{3.12}$$

where, $(R_{anc}R_{obs})_{max}$ is the maximum value of the anchor and observer distance to the target and can be given as,

$$(R_{anc}R_{obs})_{max} = \left(\frac{(R_{anc} + R_{obs})^2}{4}\right) = \frac{(R_B)^2}{4} \tag{3.13}$$

where $R_B = R_{anc} + R_{obs}$ is the bistatic range.

For a typical WRSN, each anchor node transmits their compressed pulses with minimum power level P_{min}^{anc} for accurate sensing at maximum range. Besides, this power level can be adjusted for different WRSN topologies. Moreover, in error analysis part of this paper, P_{min}^{anc} is used to show a typical error level of this system.

CHAPTER 4

COLLABORATIVE MOBILE TARGET IMAGING (CMTI)

In this chapter, we present collaborative mobile target imaging (CMTI) algorithm and its operation in detail. The objective of CMTI algorithm is to accurately and efficiently obtain an image of mobile targets based on the collaborative effort of deployed UWB wireless radar sensor nodes. First, we begin by presenting an overview of CMTI, and then the detailed operation of the CMTI algorithm is explained.

4.1 CMTI Algorithm Overview

CMTI is a five-phase algorithm. It requires that radar sensor nodes are equipped with sensors to gather radar range profile of the mobile target. All radar sensors have fixed location in the field. The hardware architecture of these radar sensors are detailed in the Section 3. CMTI algorithm is adaptive to different velocity and heading of the mobile targets and can be configured according to the required level of image quality.

The overall operation of CMTI starts with *Initialization Phase* as explained in Section 4.2. During this phase, sink selects anchor nodes, called *Head Anchor*, where *target tracking* and *inverse synthetic aperture capturing* phases are operated over the entire field. Sink also initializes all sensors in the target detection layer as shown in Fig. 3.1. Then, if any detection happens, sink awakes related radar sensor nodes in the target imaging layer at this phase.

Target tracking phase begins after initialization and continues to run to the end of the *Inverse Synthetic Aperture Capturing (ISAC) Phase*. During target tracking phase, all active anchors start to send impulses and active observers begin to measure bistatic range of the mobile target. Then, all these range measurements are sent to corresponding *Head Anchor*, which calculates the location of the mobile target with non-linear least square optimization on triangulation algorithm. A target road-map which has the mobile target location for each specific time interval, can be formed. With the use of the target road-map, *Head Anchor* can calculate the target head courses as explained in Section 4.3.

Using the target velocity and head course vectors calculated in the previous phase, the *Head Anchor* first creates a plane, i.e., *image plane*, where a UWB radar image of the mobile target is formed. In order to form a radar image, CMTI captures inverse synthetic aperture created by the movement of the target along the multi-static radar structure. Therefore, a matrix, called *Inverse Synthetic Aperture Matrix* (*ISAMatrix*), which consists all information about anchor-observer pairs whose observations are used in imaging, is formed by *Head Anchor*. This phase is called *Inverse Synthetic Aperture Capturing (ISAC) Phase* and detailed in the Section 4.4.

According to the *ISAMatrix*, *Head Anchor* asks observer nodes to provide the required observations to the sink. Then, all the observations are reliably and energy efficiently transported to the sink during *Reliable Imaging Observation Transport (RIOT) Phase* as explained in Section 4.5.

Once the observation messages are reliably received at the sink, the *ISAMatrix* is regenerated from the information conveyed in the header of the observation messages. According to the information in *ISAMatrix*, an UWB radar image of the mobile target is formed in the image plane in the final operational phase, i.e., *Imaging Phase*. After all the observations are collected, all the related anchor-observer pairs are placed to the image plane. Then, time-domain back-projection based collaborative radar imaging algorithm is applied to form a radar image. The details of the *Imaging Phase* are given in Section 4.6.

4.2 Initialization Phase

Sink initializes the overall operation of WRSN and starts with localization process. In localization process, all sensor nodes are localized through use of existing node cooperative localization techniques developed for WSN [30], [31]. Then, the entire sensor field is divided into clusters by sink using one of the energy-efficient, robust and optimum clustering schemes in the literature [32] to select *Head Anchors* in the field, which take the responsibility of tracking and inverse synthetic aperture capturing. However, in CMTI, clustering only means to project the cluster regions for easily selecting *Head Anchors* in the entire field. After specifying cluster regions, sink determines *Head Anchors* in their own clusters.

For head anchor selection, each anchor sends its location and own remaining battery lifetime to the sink. Sink looks for the spatially midmost anchor in the cluster, but if it has the worst lifetime, sink selects the second midmost anchor. Then, corresponding *Head Anchors* are specified for each clusters in the entire field and each one is responsible for the events in own cluster.

After *Head Anchor* selection is performed, sink broadcasts *start detection* message to the sensor nodes in the target detection layer of WRSN. If any event is sensed by the detection sensors, this event record is transmitted to the sink. Then, radar sensor nodes in the location of the event are woken up by sink node's *wake up* message. Once the target is detected, target tracking phase of CMTI is invoked and nearest *Head Anchor* to the event field takes the responsibility of the detection.

Observers take observations from the environment with specific time intervals. In Section 3, this time interval is presented as T_σ. These observations at one interval compose one *frame*. At this point, we use *frame* as time interval two consecutive complete observation. Hence, according to the frequency of the frame, observers continue to take observations from the environment frame by frame in entire CMTI process. Frames are used in tracking process and only few of them are used for imaging process. If a frame is used in imaging process, we called it as *picture*. Therefore, each *picture* used in CMTI can be taken with different frequency.

4.3 Target Tracking Phase

Target Tracking Phase is operated concurrently with *ISAC Phase*.

After *wake up* message is broadcasted by sink, each anchor broadcasts its own location to the observers in its own radar range. Therefore, each observer knows whose impulse can reach to itself and what is their distance to corresponding anchors.

In CMTI, tracking is operated in two dimensional (2D) coordinates. For 2D tracking, obviously only 3 ellipsoid equation is enough to determine the location of the target. Hence, as long as,

$$N_{anc}N_{obs} \geq 3 \tag{4.1}$$

where N_{anc}, N_{obs} are the number of the awake anchors and observers in the event field respectively, all observer nodes start to determine the mobile target distance with time difference of arrival (TDoA) measurements from target. Then, observers pack the time and range measurement data up and send all to the *Head Anchor* to be used in the tracking process.

In order to make target localization, *Head Anchor* begins to collect all the range measurements from the alerted observers for one second with the frame frequency, F_t, such that the first F_t target location suffice to reveal the target mobility behavior such as the velocity.

In this phase, the mobile target locations are calculated frame by frame and then mobile target velocity is computed to update the frame frequency, according to the target locations and corresponding frame time tags.

At the *Head Anchor*, using the received $F_tN_{anc}N_{obs}$ range measurements, target location (u_x^i, u_y^i) in frame i is calculated with non-linear least square optimization on triangulation algorithm [29].

To this end, let R_{anc}^g be the distance of anchor g to target in frame i, i.e.,

$$R_{anc}^g = \sqrt{(x_g^i - u_x^i)^2 + (y_g^i - u_y^i)^2} \tag{4.2}$$

where (x_g^i, y_g^i) is the g^{th} anchor location at frame i.

Observer to target location (R^w_{obs}) is,

$$R^w_{obs} = \sqrt{(x^i_w - u^i_x)^2 + (y^i_w - u^i_y)^2} \tag{4.3}$$

where (x^i_w, y^i_w) is the w^{th} observer location at frame i.

Using (12) and (13), the ellipsoid range function is obtained as,

$$F(u^i_x, u^i_y) + \epsilon = (R^g_{anc} + R^w_{obs}) \tag{4.4}$$

where $(R^g_{anc} + R^w_{obs})$ is the related range and ϵ is the random and typically small range error.

Non-linear least square estimation of the range equation is a value (u^i_x, u^i_y) which minimizes the sum, i.e.,

$$argmin_{u^i_x, u^i_y} \sum_{Available\ Perspectives} (F(u^i_x, u^i_y) - (R^g_{anc} + R^w_{obs})) \tag{4.5}$$

Thus, the target location in the event field with non-linear least square optimization of triangulation algorithm can be obtained through Taylor Series (TS) method [29]. Then, the velocity of the target is calculated by the *Head Anchor*, according to these triangulation results to specify the new frame frequency.

Note that the required frame frequency (F_t) for successful tracking process depends on the velocity of the mobile target. Each anchor-observer pair has a certain radar range resolution, which is defines as an ability to resolve point targets that are separated in range to the radar [9], and target mobility under this range resolution cannot be observed. Therefore, the frame frequency, F_t, can be adapted according to the target velocity as follows,

$$F_t \geq \frac{V_T}{cPW/2} \tag{4.6}$$

where V_T is the target speed and PW is the anchor pulse-width. After finding the target velocity, the new frame frequency calculation is done by *Head Anchor*. Then, this frequency is sent by *Head Anchor* to the observers. Observers continue to pack the time and range measurement data up with updated F_t and send all to the *Head Anchor* for the tracking process. Meanwhile, all observers begin to record their

observations with time tag, and then they keep these records until the sink requests in imaging phase.

At the *Head Anchor*, with F_t, the target location at each frame continues to be calculated with non-linear least square optimization on triangulation algorithm.

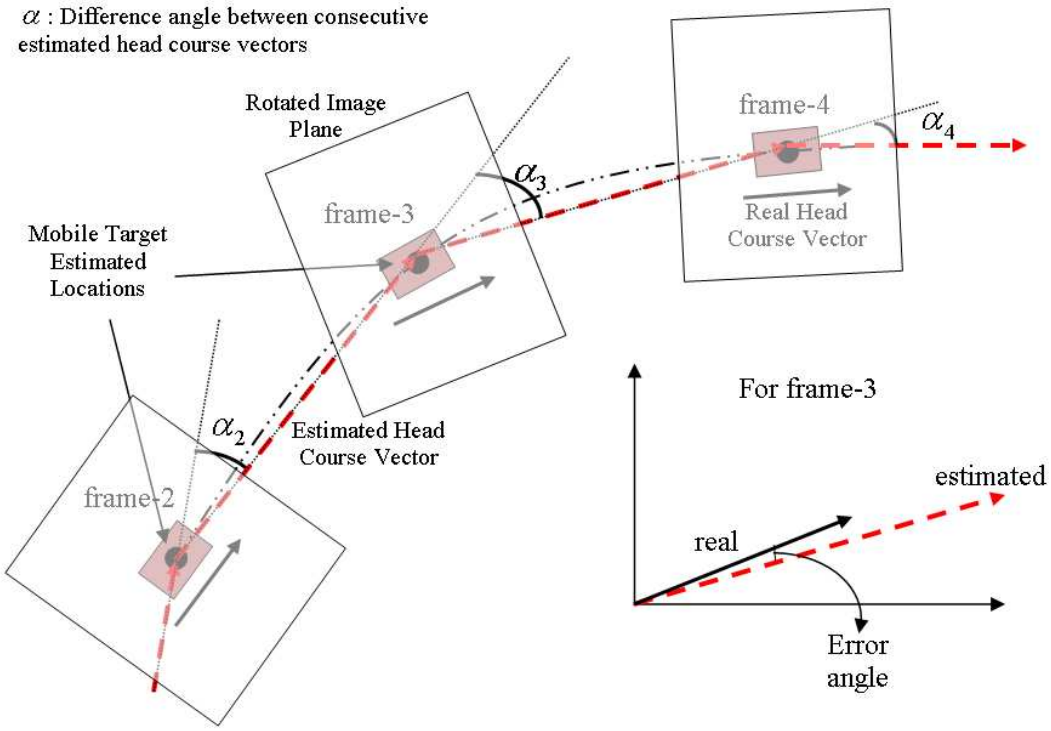

Figure 4.1: Head Course Calculation

After mobile target localization, head course vectors, which indicate the heading of the target for each frame, are calculated and recorded to be used for *ISAC Phase*. If the target velocity does not have constant direction in the time between two consecutive frames which is $(cPW)/(2V_T)$ from (4.6), the target head course vectors must be specified in CMTI.

After the mobile target estimated locations for each frame is obtained in *target tracking phase*, in order to find estimated head course vectors, each location is processed with the proceeding frame location of the target. Estimated head course vectors can be drawn as a vector from n^{th} to $(n+1)^{th}$ target location point and real

head course vectors show the direction of mobility of the target as seen on the Fig. 4.1. Hence, there should be $(n + 1)$ frame must be used to estimate head courses for each frame, when total head course vector number is n. Note that, in order to prevent forming blurry radar images with CMTI algorithm, the direction of mobility and target head course vector are assumed to be in the same direction for each frame.

The head course vectors are calculated by *Head Anchor* for each frame. According to the difference angle between consecutive estimated head course vectors, α, the image plane is moved and rotated with respect to the direction changing on the consecutive head course vectors frame by frame as seen on Fig. 4.1.

4.4 Inverse Synthetic Aperture Capturing (ISAC) Phase

In this phase, $ISAMatrix$, which is 4 by 360 matrix consists anchor and observer numbers, whose observations are used in *Imaging Phase*, with related picture number with respect to the corresponding bistatic bisector angle, is filled by *Head Anchor* of the cluster in alert.

The bistatic bisector angle, θ, the bistatic angle, β, and anchor-observer distance, L, are showed in Fig. 4.2.

Image plane, where the target radar image is formed, can be determined from the target locations and head course vectors, in the way that the target must be in the middle of this plane. Then, the image plane is moved and rotated hypothetically by the *Head Anchor* to find θ for each observation, with respect to the difference angles, α, frame by frame as seen in 4.1.

As said before, each anchor-observer pair composes a bistatic radar structure. In this phase, the anchor-observer pairs which contribute most towards maximizing the quality of the radar image are selected. The ISAC Algorithm in CMTI is also outlined in Algorithm 1.

Note that, radar range resolution (ΔR) mainly dominates the quality of the radar image. The bistatic range resolution, ΔR_B, of any anchor-observer pair varies with respect to the bistatic angle β, which is the angle between anchor-observer pair with the virtex at the target [11] as seen in Fig. 4.2.

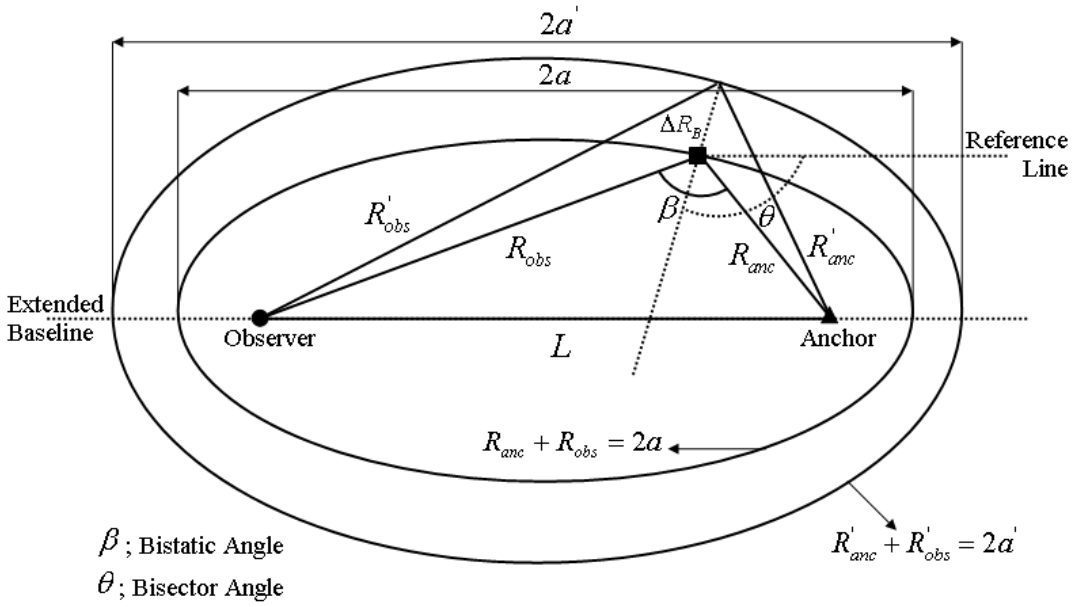

Figure 4.2: Bistatic Radar Structure

CMTI gets observations with random perspectives. Therefore, anchor-observer pairs are placed into the $ISAMatrix$ with respect to their bistatic bisector angle (θ) to the target. Bistatic bisector angle is an angle between a line that bisects the bistatic angle and a reference line as seen on the Fig. 4.2.

For a radar image, all observed perspectives can be taken for imaging, however, some of them may cause quality degradation in the radar image. Therefore, algorithm should select the best anchor-observer pairs for each perspective.

In *ISAC Phase*, anchor-observer pairs with the smallest bistatic range resolution are selected to be included in the image formation process. For a monostatic radar case, the range resolution is $\Delta R_M = cPW/2$. However, for a bistatic case, this relation becomes for approximate method [11],

$$\Delta R_B = \Delta(R_{anc} + R_{obs}) \approx \frac{cPW}{2cos(\beta/2)} \tag{4.7}$$

where β is the bistatic angle as seen in Fig. 4.2. As seen clearly on (4.7), depending on the β angle, range resolution increases. Here, in order to find more accurate

bistatic range resolution for higher β, CMTI adopts another approximate expression in [23] to calculate the bistatic range resolution. Approximate expression is given by,

$$\Delta R_B \approx \frac{cPW\sqrt{R_{anc}R_{obs}}}{\sqrt{(R_{anc}+R_{obs})^2 - L^2)}} \tag{4.8}$$

and L can be given as,

$$L = \sqrt{R_{anc}^2 + R_{obs}^2 - 2R_{anc}R_{obs}cos(\beta)} \tag{4.9}$$

then substituting (4.9) into (4.8), bistatic range resolution can be found as,

$$\Delta R_B \approx \frac{cPW}{\sqrt{2(1+cos(\beta))}} \tag{4.10}$$

Then, according to the bistatic radar range resolution, CMTI algorithm selects appropriate anchor-observer pairs, which have the smallest range resolution, for each bisector angle to the target. Besides, in order to prevent selecting pairs which have very large range resolution, CMTI defines a threshold for ISAC algorithm to discard inappropriate pairs. Selecting the best threshold is out of the scope of this thesis, however, in our simulations show that, the threshold on the range resolution can be selected as cPW. This selection component is called *Smallest Range Resolution Selection with Threshold* (SRRS-th) and it provides radar imaging without deformations.

When the mobile target moves along the sensor field, CMTI captures the inverse synthetic aperture of the WRSN. Then, according to the smallest range resolution selection with threshold (SRRS-th) component, $ISAMatrix$ is filled with anchor and observer numbers picture by picture.

After filling $ISAMatrix$, head anchor try to decide the size of the each observation to be transferred to the sink. In CMTI, all parts of the observation does not have valuable information for the imaging of the mobile target. Only target radar response part of the observation is important for target imaging. With moving target filter at the observer, target radar response can be distinguished from entire observation to specify target features. As explained in the *target tracking phase*, observers

can measure the distance of the target. Hence, observers can make a window around the target radar response with using the distance measurement results. For CMTI, we propose a time-domain window, called *target observation window*, W, on the target radar response of each observation to decrease communication overhead of WRSN.

In order to specify W length, head anchor looks the range measurement data used in *target tracking phase* and selects the ones used in $ISAMatrix$. If any of the range measurement cannot be found by head anchor, head anchor requests this measurement from the observer which holds the missing range measurement. From the range measurements, head anchor calculates the longest target range profile. After that, depending on the longest range profile, it decides the target observation window length W. Head anchor broadcasts the W length to all alerted observers.

According to the anchor, observer and picture numbers in the $ISAMatrix$ and W length, head anchor informs the alerted observers with sending the number of which observations to be sent to the sink.

4.5 Reliable Imaging Observation Transport (RIOT) Phase

After *ISAC Phase*, in this phase, all observers reliably send their recorded observations to the sink. In this way, target radar image can be constructed with high quality at the sink. At the same time, energy efficiency of the sensor network must be considered, because of the resource constraints of the radar sensor nodes. Hence, energy efficiency needs to be considered along with high quality mobile target imaging in WRSN.

In CMTI operation, three types of packets, i.e., observation transport packets (OTP), range measurement packets (RMP), and CMTI control packets (CCP) are used as in Fig. 4.3.

Observation Transport Packets (OTP) carries the imaging observations to the sink, with perspective number, anchor and observer number, picture number and location of the packet in entire observation. If observation size (l_{OBS}) is larger than the packet size, entire observation is divided into small blocks with length (k). Each block with $7Byte$ header as seen in Fig. 4.3. Packet location (PL) bytes are used

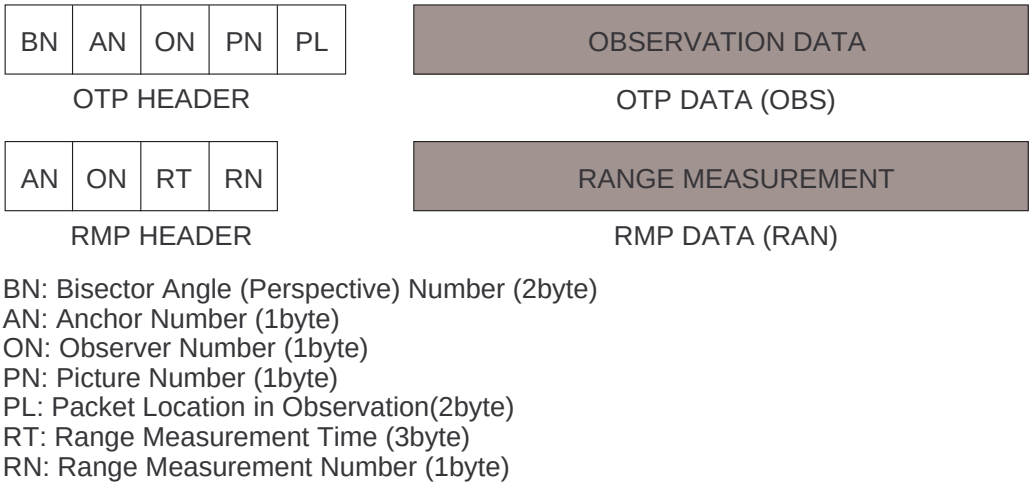

Figure 4.3: CMTI Packet Format (OTP and RMP)

to indicate where the location of the packet in the observation. The OTP Header also contains a byte which indicates the observation perspective number (BN). BN denotes in which bistatic bisector angle the target is observed. AN,ON and PN fields are used for sending $ISAMatrix$ information as anchor, observer and picture number, respectively.

Range Measurement Packets (RMP) carries target distance, anchor and observer number. It includes $6byte$ header part with the information which anchor-observer pair measure that range as seen in the Fig. 4.3. The rate of this packet is specified with control packets by head anchor node in the tracking phase. RMP is sent from observers to head anchor node which is generally at one hop distance.

CMTI Control Packets (CCP) provides the control of the entire CMTI process and is used for informing observers transition times between CMTI phases. CCP is also used to inform observers for the new frame frequency or for alerted anchor node specific codes.

In the literature, if we consider retransmission for upstream reliability, there are many protocols proposed for WSN for event and packet reliability [28]. ESRT (Event-to-Sink Reliable Transport) works for guaranteeing event reliability through

end-to-end source rate adjustment and requires no packet reliability [41]. However, in CMTI, each observation is independent from each other and has the same importance for radar imaging. On the other hand, RMST (Reliable Multi Segment Transport) [40] and RBC (Reliable Bursty Convergecast) [42] aim to reach very high packet reliability for high number of data transportation through hop-by-hop retransmission-based loss recovery. However, in CMTI, size of data which is sent to sink at each observer is not very high and reliability requirement is not very high for CMTI. That is to say, neither of them seems to be well suited for reliable imaging observation transportation with CMTI.

In fact, performance comparison between retransmission and forward error correction (FEC)-based mechanisms has been given in the literature [33], [34] and [35]. According to [33], link-level retransmission is efficient, but limited for providing high reliability. Hence, erasure codes can handle high reliability with tolerating packet losses [33]. In [34], a theoretical work is done to specify the effects of retransmission and forward error correction (FEC) on transmission reliability and energy efficiency of WSN. The analysis in [34] shows that for low bit-error rate channel, erasure coding is both energy-efficient and more reliable. However, for high packet error rate condition, erasure codes compromise energy efficiency for reliability.

With this regard, for reliable imaging observation transport (RIOT) phase, retransmission-based automatic repeat request (ARQ) and forward error correction (FEC) approaches are compared in terms of energy efficiency [38] in Appendix A. Here, different FEC coding mechanisms are explored compared to ARQ performance, and the numerical results revealed that FEC (e.g.,with Reed Solomon RS(63,53,5)) could be used to achieve high energy efficiency and reliable delivery of observer measurements.

In CMTI, for realizing FEC based reliable transportation of observations, we assume that each radar sensor node hardware includes RS encoder and decoder. However, sink includes only RS decoder.

Finally, sink receives all observation transport packets (OTP) coming from distributed observers, and then, according to anchor-observer pair number and perspec-

tive number in the observation header of each OTP, sink regenerates the $ISAMatrix$. Definitely, some packets may be lost due to network or channel related packet losses, and observations can be reconstructed to a certain extent with the help FEC scheme. Nevertheless, some observations may not be reconstructed due to high packet loss probability on the channel. However, a small decrease on the number of observations cause only small degradations on the radar image, and this degradations may not affect the classification of the mobile target from the radar image.

4.6 Imaging Phase

2D image of the target is required to specify shape and features of it. 1D profile of the target can be easily extracted from time-domain calculation of received signal using only range-profile of the target, but the second dimension involves more calculation on frequency-domain using Doppler-profile of the target [9], [10]. However, obtained range profiles with different perspectives of the target can be used to form 2D image. In this phase, instead of frequency-domain calculations to extract the second dimension, radar images are created by CMTI based on *kirchhoff migration* [20], which is the one of the well known time-domain imaging methods.

In the imaging phase, *kirchhoff migration* techniques as *standard back-projection* (*SBP*), *cross-correlated back-projection* (*CBP*) [19] and its modified version [20] are used to form radar images. These algorithms are suitable for the multi-static radar imaging structures [13]. The overall operation of the imaging phase of CMTI is outlined in Algorithm 2.

Basic principle of the *SBP* is coherent sum of sampled radar returns of array elements [19]. The *SBP* algorithm projects the spatial coordinates of transmitter and receiver antenna to the image plane, and then, correlates transmitter, receiver and the pixel to the range profiles of receivers. This yields acceptable results in short-range applications. However, for larger distances, the *SBP* approach produces smeared images [19].

On the other hand, *CBP* algorithm yields a better cross-range by correlating the range profiles. It generates a signal for the specific pixel location by coherent

sum of cross-correlation between the main channel and the reference channel. The resulting signal eliminates the smearing at the *SBP* image [19].

In this phase, after receiving observations reliably as explained in Section 4.5, the size of the area to be displayed in the image plane is decided. Then, perspectives are selected by checking the first row of the $ISAMatrix$. Image plane width and length are specified in pixels. Due to each pixel location (i, j), the time of flight (ToF) of pulses are calculated for each perspective. Amplitude of the received signal from the anchor of the observer at the corresponding ToF for the picture is recorded. After that, in order to correlate channels, a reference channel should be specified. For this purpose, a reference observer is selected from the other observers, of which pulses are transmitted from the same anchor at the same picture. However, the selection is made on the verticalness of the perspective to anchor-observer pair. Moreover, for using the modified version of CBP, CMTI algorithm finds additional reference observer. Then, recorded observation signals from three channel are cross-correlated for the pixel (i, j) and then cross-correlated value is saved. The saved values are summed for each perspective. After all perspectives are processed for pixel (i, j), the result of this sum is assigned to the value of the pixel (i, j). After all, this process is repeated for each pixel on the entire image. Then, the radar image of the mobile target is formed.

Algorithm 1: ISAC Algorithm (SRRS-th) in WRSN Structure. α and γ are the angles between the anchors and observers LOS to target and reference line in a specific frame. $BiRes$ is the bistatic range resolution matrix which consists of all anchor-observer pairs bistatic range resolutions with a specific picture. $noanc$, $noobs$, and $nopic$ are total number of anchor nodes and observer nodes, and picture, respectively.

$ISAMatrix = zeros(4, 360)$
$BiRes = zeros(nopic, noanc, noobs)$
for $h = 1 : nopic$ **do**
  for $g = 1 : noanc$ **do**
    α=CalcLOS(g^{th}, h^{th})
    for $w = 1 : noobs$ **do**
      γ=CalcLOS(w^{th}, h^{th})
      /*Find bisector angle θ*/
      $\theta = (\alpha + \gamma)/2$
      /*Find bistatic angle β*/
      $\beta = (\alpha - \gamma)$
      $BiRes(h, g, w) = (c \times PW)/(sqrt(2(1 + cos(\beta))))$
      if $BiRes(h, g, w) > (c \times PW)$ **then**
        /*Not use anchor-observer pair*/
        go to next iteration
      end
      if $ISAMatrix(1, \theta) == 1$ **then**
        $w_{ex} = ISAMatrix(2, \theta)$
        $h_{ex} = ISAMatrix(3, \theta)$
        $g_{ex} = ISAMatrix(4, \theta)$
        /*Select the Smallest Range Resolution*/
        if $BiRes(h, g, w) < BiRes(h_{ex}, g_{ex}, w_{ex})$ **then**
          $ISAMatrix(2, \theta) = w$
          $ISAMatrix(3, \theta) = h$
          $ISAMatrix(4, \theta) = g$
        end
        go to next iteration
      end
      $ISAMatrix(1, \theta) = 1$
      $ISAMatrix(2, \theta) = w$
      $ISAMatrix(3, \theta) = h$
      $ISAMatrix(4, \theta) = g$
    end
  end
end

Algorithm 2: Imaging phase of CMTI algorithm. DISTANCE function only calculates geometric distance in pixels. $DiffSig$ is the motion filtered recorded signal from the observer.

```
/*Find available perspectives*/
I=Find(ISAMatrix(1,:) == 1)
pxlres=100ns/400pxl; Fs=20Gsps; PW=0.5ns;
foreach pixel (i, j) do
    counter = 0
    sumtemp = 0
    for k = 1 : LENGTH(I) do
        obs = ISAMatrix(2, I(k)) /*specify observer number*/
        pic = ISAMatrix(3, I(k)) /*specify picture number*/
        anc = ISAMatrix(4, I(k)) /*specify anchor number*/
        ToF_pa=DISTANCE((i,j),(anc at pic))*(pxlres)
        ToF_po=DISTANCE((i,j),(obs at pic))*(pxlres)
        DiffSigMain = DiffSig(obs, pic, anc, :)
        if ((ToF_pa + ToF_po) ≤ 100ns) then
            objloc = (ToF_pa + ToF_po) * Fs
            /*calc. loc. of the pulse reflected from object in recorded signal */
            NORMALIZE(DiffSigMain, objloc)
            SigMain = DiffSigMain(objloc-(PW/2):objloc+(PW/2))
        end
        /*reference observer finding process started*/
        Cond1 = (ISAMatrix(2, I) ≠ obs)
        Cond2 = (ISAMatrix(3, I) == pic)
        Cond3 = (ISAMatrix(4, I) == anc)
        I_obs=Find(Cond1&Cond2&Cond3)
        if isempty(I_obs) then
            go to next pixel
        end
        I_z=Find(observer vertical to obs relative to anc)
        obsref = ISAMatrix(4, I_obs(I_z(1)))
        DiffSigRef = DiffSig(obsref, pic, anc, :)
        ToF_ref=DISTANCE((i,j),(obsref at pic))*(pxlres)
        if ((ToF_ref + ToF_pa) ≤ 100ns) then
            objloc = (ToF_ref + ToF_po) * Fs
            NORMALIZE(DiffSigRef, objloc)
            SigRef = DiffSigRef(objloc-(PW/2):objloc+(PW/2))
        end
        Signal = SigMain * SigRef
        sumtemp=INTEGRATE(Signal)+sumtemp
        counter = counter + 1
    end
    Image(i, j) = log10((1/counter) * sumtemp)
end
```

CHAPTER 5

CMTI ERROR ANALYSIS

In this chapter, we analyze CMTI in detail and point out the sources of error which may affect the obtained radar image quality. We first analyze the ranging process, and then, the radar imaging with respect to the range resolution.

One anchor-observer pair corresponds to a bistatic radar structure. Therefore, we perform our analysis considering this bistatic radar structure.

Noise is the main limitation of radar measurements. Receivers must have large signal to noise ratio (SNR) for accurate measurements. $R_B = (R_{anc} + R_{obs})$, the distance of anchor-target-observer multi-path, is the measurement of time delay for the anchor's radar signal, which travels out from the target to the observer. Assuming that there is no error on the propagation speed of light in the medium, the error on the range is, $\delta R_B = c\delta T$, where δT is the time delay error and c is the speed of light.

First of all, the ranging process is based on time-delay measurement which is the time-difference between anchor to observer direct signal and anchor-target-observer multi-path signal. Moreover, this time difference of arrival (TDoA) measurement strictly depends on the observer side SNR. Hence, the error on range measurement can be calculated with respect to the SNR value.

Using the expression in (3.3), the SNR in the bistatic radar structure can be expressed as [14],

$$SNR_{Bistatic} = \frac{P_{anc}C}{(R_{anc}R_{obs})^2} \tag{5.1}$$

where C is a radar constant i.e.,

$$C = \frac{N_s G_{anc} G_{obs} \sigma_B c^2}{N_0 PRF (4\pi)^3} \left(\frac{1}{f_L} - \frac{1}{f_L + B} \right) \tag{5.2}$$

In radar sensor nodes hardware configuration, PRF and antenna gains of both nodes are constant, and hence, C is constant. Therefore, SNR depends only on P_{anc} and $(R_{anc} R_{obs})$.

The measure of time-delay error is the root mean square error (rms) of the difference between the measured value and the true value. In, the theoretical rms error of the time-delay measurement can be stated as [8],

$$\delta T = \frac{1}{\chi \sqrt{2SNR}} \tag{5.3}$$

where χ is the effective bandwidth of the received waveform and expressed as [8],

$$\chi^2 = \frac{\int_{-\infty}^{\infty} (2\pi f)^2 |S(f)|^2 \, df}{\int_{-\infty}^{\infty} |S(f)|^2 \, df} \tag{5.4}$$

In anchor UWB transmitter architecture, normal Gaussian pulses are transmitted and after the observer antenna, the second derivative of the transmitted pulses are received, because of the effect of the antenna and the channel. In error calculation, a typical value for the compressed Gaussian pulses effective bandwidth is used as $5.2/PW$, where PW is the pulse-width.

For all points on a equi-ToA ellipse, SNR is not constant. According to the bistatic angle β, SNR can vary and thus, error on the range measurement varies. Bistatic SNR of any anchor-observer pair is illustrated as in Fig. 5. In order to find maximum error, it is calculated as β is maximum. Hence, when β is maximum, R_{anc} is equal to R_{obs}, and then, $(R_{anc} R_{obs})$ can be expressed as $(R_B)^2 / 4$. The rms error of range measurement is $c \times \delta T$ and can be expressed by substituting (5.1) into (5.3),

$$\delta(R_{anc} + R_{obs}) = \frac{c (R_B)^2}{4\chi \sqrt{2 P_{anc} C}} \tag{5.5}$$

In order to observe the range measurement error incurred during the ranging process, we now plug typical UWB radar sensor parameters as in the Table 5.1 into

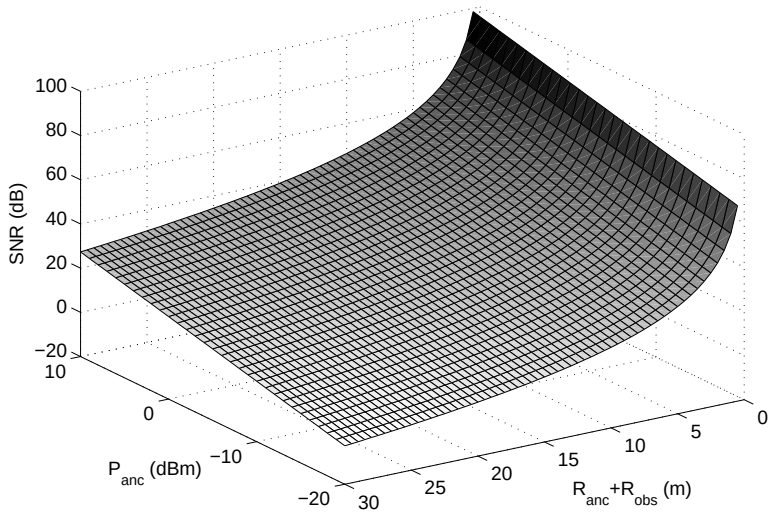

Figure 5.1: Bistatic SNR at Observer vs. Transmitted Power, Bistatic Range

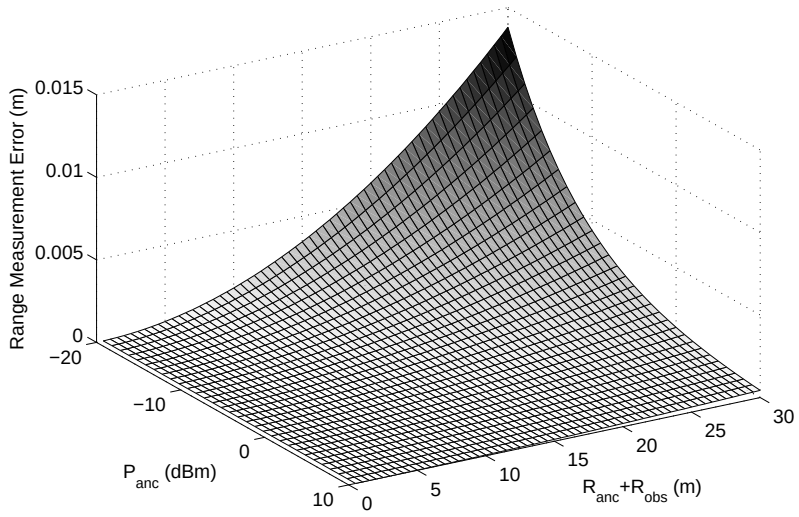

Figure 5.2: Range Measurement Error vs. Transmitted Power, Bistatic Range

(5.5). The range measurement error versus P_{anc} and (R_{anc} + R_{obs}) are shown on the Fig. 5.2. Hence, if P_{anc} is selected closer to the $-20dBm$, then the ranging error

becomes nearly 1.4cm at maximum range 30m. For the values in the Table 5.1, P_{min}^{anc}, explained in Chapter 3, can be found as $0.184mW$, $-7.35dBm$. Therefore, when P_{min}^{anc} is transmitted at anchor, only 3mm ranging error is observed at 30m maximum bistatic range as in the Fig. 5.4.

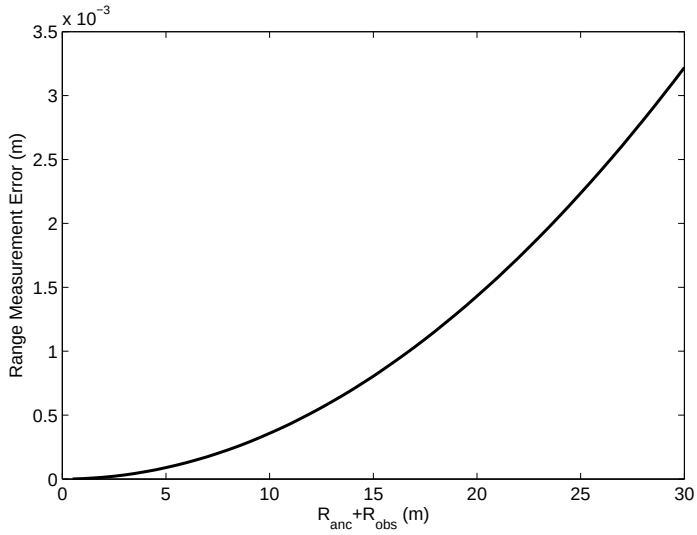

Figure 5.3: Range Measurement Error for P_{min}^{anc} vs. Bistatic Range at Maximum β Angle

Another source of error on the CMTI is the *range resolution error*. This error shows the difference between monostatic and bistatic radar resolutions which directly affect radar image quality. This normalized error can be expressed as,

$$\epsilon = (\Delta R_B - \Delta R_M) \,/\, (\Delta R_M) \tag{5.6}$$

where ΔR_M is the monostatic range resolution. ΔR_B is the bistatic range resolution and expressed in Section 4.4.

As seen on Fig. 5.4, as β approaches 180 degrees, the range resolution error significantly increases. Therefore, CMTI selects anchor-observer pairs which has a smaller bistatic angle β.

In CMTI, to reduce the distortion on the radar image, there is a smallest range

resolution selection with threshold (SRRS-th) algorithm with respect to the bistatic angle β considering the range measurement and range resolution error explained in Section 4.4.

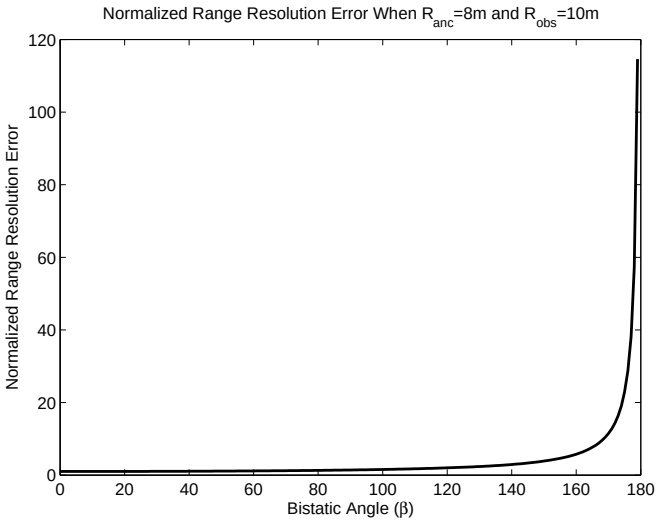

Figure 5.4: Normalized Range Resolution Error vs. β

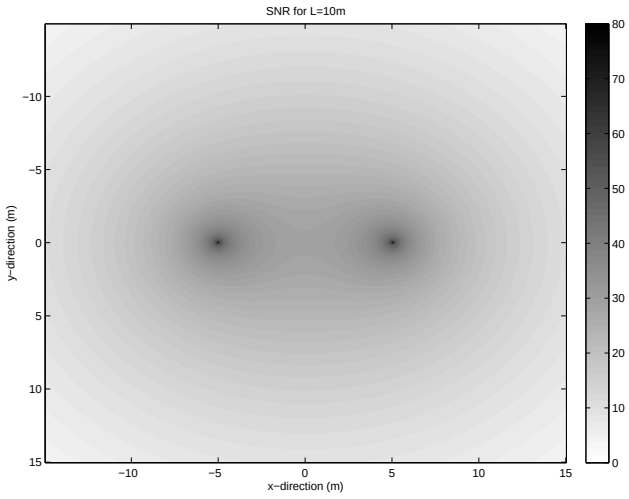

Figure 5.5: Bistatic SNR for Anchor-Observer Pair for $L = 10m$

Table 5.1: Typical UWB Radar Sensor Parameters

Parameters		
Symbol	***Definition***	***Quantity***
RG_w	observer range-gate width	$50ps$
PW	anchor pulse-width	$0.5ns$
R_{max}	maximum bistatic range	$30m$
B	Bandwidth	$2GHz$
f_L	lower frequency	$1.5GHz$
f_U	upper frequency	$3.5GHz$
N_s	processing gain	$10dB$
G_{anc}	anchor antenna gain	$0dB$
G_{obs}	observer antenna gain	$0dB$
SNR_{th}	threshold SNR	$10dB$
S_{max}	maximum number of sample	2000
V_{max}	maximum sensible velocity	$28m/s$
F_{ADC}	A/D converter sampling rate	$1.5MHz$
T_σ	time for complete signal	$1.33ms$
T_s	observer receiver temp.	$290K$
NF	observer receiver noise figure	$7dB$
N_0	noise power at the observer	2×10^{-20}
PRF	anchor pulse repetition frequency	$1.5MHz$
V_{max}	maximum sensible target velocity	$28m/s$
P_{min}^{anc}	minimum anchor transmitted power	$-7.35dB$

CHAPTER 6

PERFORMANCE EVALUATION

In this chapter, we present simulation experimental results evaluating the performance of CMTI algorithm. In the simulations, $150m \times 150m$ 2D WRSN topology is used. Radar sensor nodes are uniformly distributed over the sensor field with the anchor to observer ratio of 25%. $150m \times 150m$ sensor field is mapped to a 2000×2000pixels. The mobile target is modeled by point scatter model [24].

An ultra-wideband radar is simulated, as a 0.5 nanosecond compressed Gaussian impulses are generated by anchors with power P_{anc}^{min} and received by each observer impulse receiver with free space conditions in the event field. Radar sensor parameters are used as in the Table 5.1. Then, each corresponding received signal is processed according to these parameters.

Performance evaluations are done with respect to the selection component of CMTI, as smallest range resolution selection with threshold (SRRS-th). However, in order to show its performance, smallest range resolution selection without threshold (SRRS) and no selection on range resolution (NoSEL) algorithms are operated with SRRS-th.

In the simulations with respect to average sensor density, a 1-point mobile target is moved along sensor field, which is deployed with 8 to 20 sensors, for $10s$ with the $2m/s$ velocity, when picture frequency, F_p, is $1Hz$. Moreover, in simulations with respect to mobile target velocity, a 1-point mobile target is moved along sensor field, which is deployed with 12 sensors, for $10s$ with the velocities $1m/s$ to $28m/s$,

when F_p is $1Hz$. End-node to sink distance is $200m$ and hop count to sink node is 10.

Here, first imaging performance of CMTI is investigated with different target point scatterer models, and then, for varying radar sensor density and mobile target velocity, CMTI algorithm performance is explored in terms of four metrics, i.e., *average range resolution*, *tracking mean square error*, *communication overhead* and *energy consumption*. All radar nodes are assumed to be static. The results are shown in Fig. 6.1, 6.2, 6.3, 6.4, 6.5 and 6.6. Each data point on the plots represents a single run of the simulation. A line fitting of the data points is overlaid on each plot.

6.1 Imaging Performance

This section includes results of the CMTI with different target point scatterer models.

The first one is 1-point target. 1-point target is on a linear road with the velocity $2m/s$. In this simulation, 10 pictures are used for imaging during 6 seconds and the mobile target is tracked with only average $2cm$ error in the field. All anchors and observers are distributed uniformly over the event field, and 13 anchors and 29 observers are alerted in the field.

We run simulations for showing the difference on CMTI with and without SRRS-th which is introduced in the Section 4.4. For the configuration above, simulation is run with NoSEL, SRRS and SRRS-th components.

The non-windowed results of CMTI algorithm with selection components NoSEL, SRRS and SRRS-th, showed in Fig. 6.1, 6.2 and 6.3, are 400×400 pixels radar images which span $30m \times 30m$ field. These radar images are formed with SBP based imaging algorithm, so they have very high side-lobe values around the point. In Fig. 6.1, 6.2 and 6.3, observers and anchors locations relative to target location at first picture are indicated. In Fig. 6.1 and 6.2, obviously the side-lobe values are so high and the point can be hardly recognized in the middle of the images. On the other hand, the resulting windowed images for NoSEL, SRRS, SRRS-th with imaging algorithm based on modified CBP are shown in Fig. 6.4, 6.5 and 6.6. Obviously,

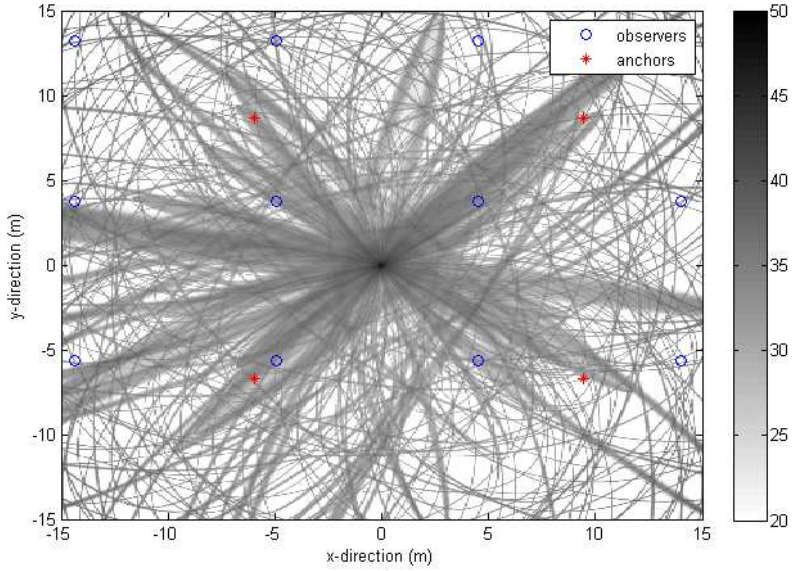

Figure 6.1: 1-Point Moving Target Radar Image with SBP based CMTI with NoSEL

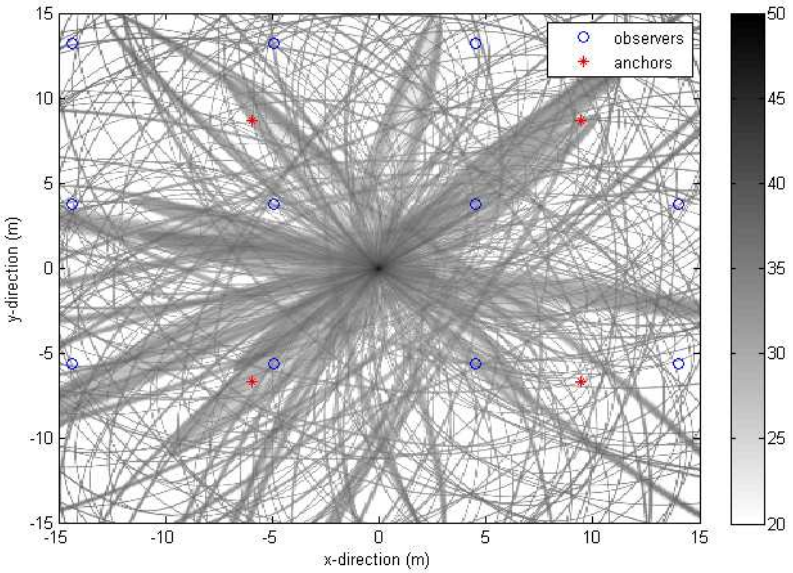

Figure 6.2: 1-Point Moving Target Radar Image with SBP based CMTI with SRRS

NoSEL totally ruins the radar image, because many anchor-observer pairs have very high bistatic range resolutions. Besides, SRRS radar image has higher quality than

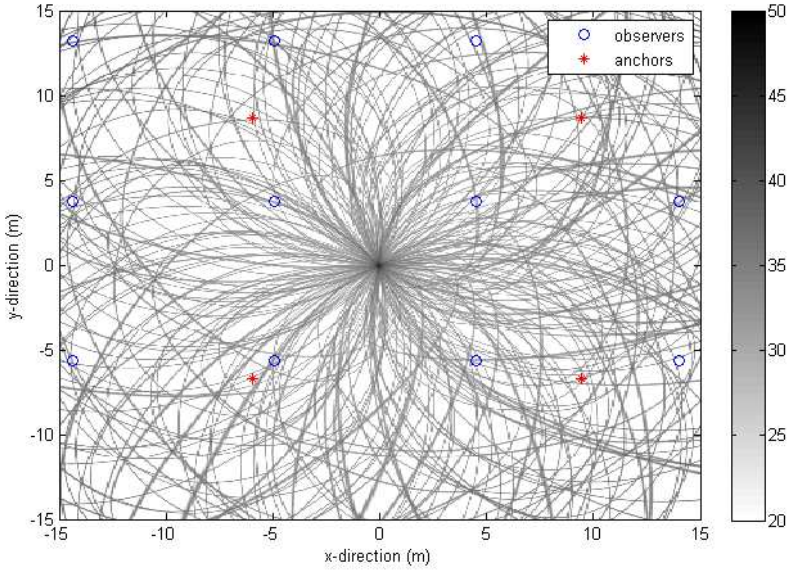

Figure 6.3: 1-Point Moving Target Radar Image with SBP based CMTI with SRRS-th

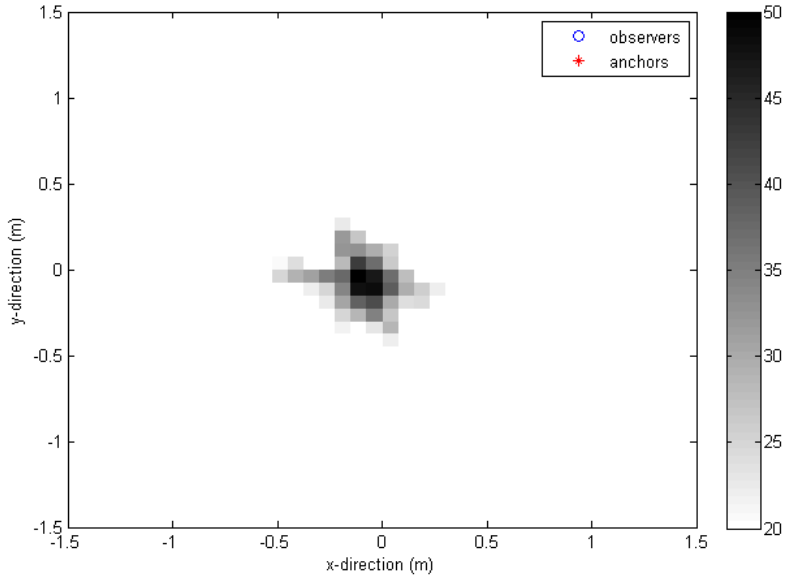

Figure 6.4: 1-Point Moving Target Radar Windowed Image with modified CBP based CMTI with NoSEL

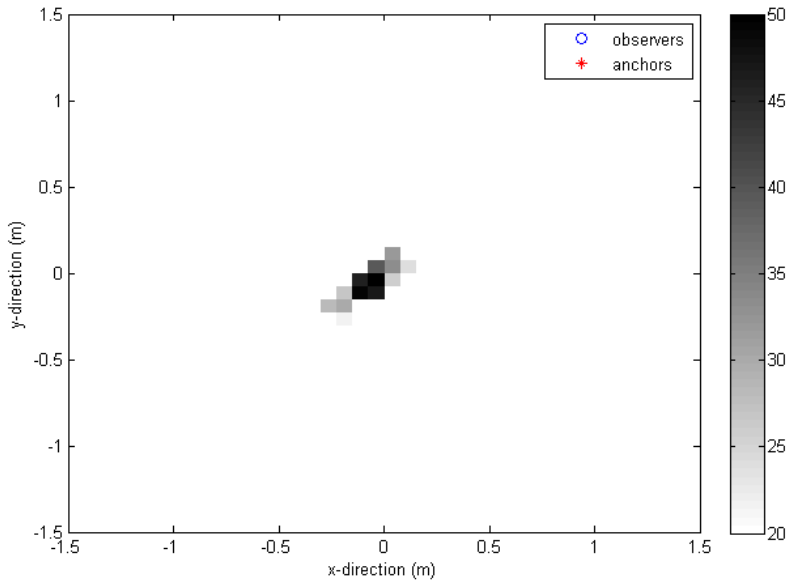

Figure 6.5: 1-Point Moving Target Radar Windowed Image with modified CBP based CMTI with SRRS

NoSEL, however, only few anchor-observer pairs degrade the image. On the other hand, SRRS-th radar image has the highest quality and the target can be clearly seen in the windowed radar image on Fig. 6.6.

As we can see on the windowed radar images, they can be used for specifying the features of mobile target. In addition to that, windowed radar image requires smaller amount of data and in this way, it adds lower communication overhead to WRSN.

With 3,5 and 17 points target models, CMTI with SRRS-th component is applied to show the performance of CMTI as in the Fig. 6.7, 6.8 and 6.9. As seen in Fig. 6.7, 6.8 and 6.9, increasing on the mobile target dimension results larger radar image size, because CMTI increase target window size from small target to larger target. For the 3 and 5 points targets, each point can be clearly distinguished from other points in Fig. 6.7 and 6.8. Besides, for 17 points target its shape and dimensions can be extracted from the image in Fig. 6.9.

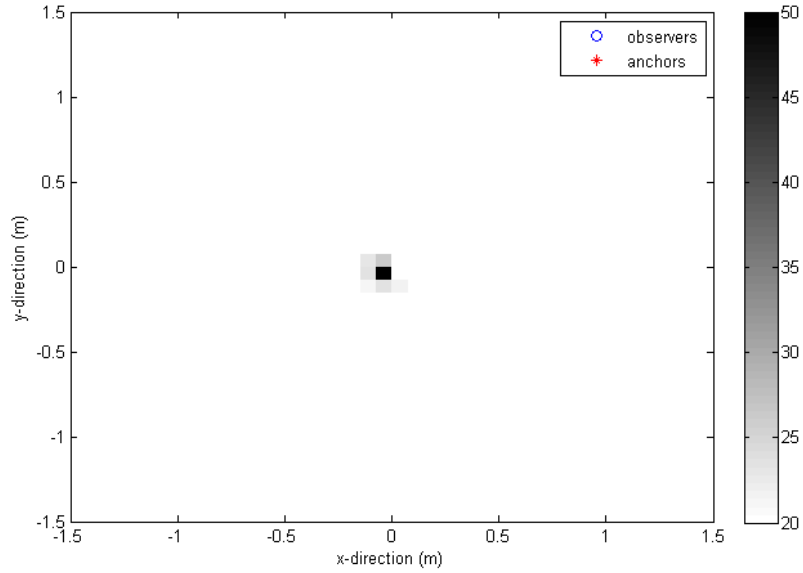

Figure 6.6: 1-Point Moving Target Radar Windowed Image with modified CBP based CMTI with SRRS-th

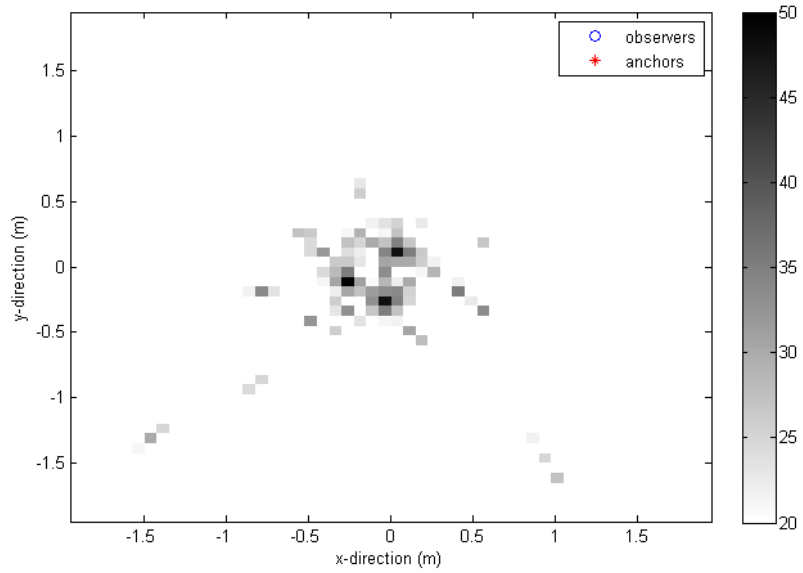

Figure 6.7: 3-Point Moving Target Radar Windowed Image with Modified CBP Based CMTI with SRRS-th

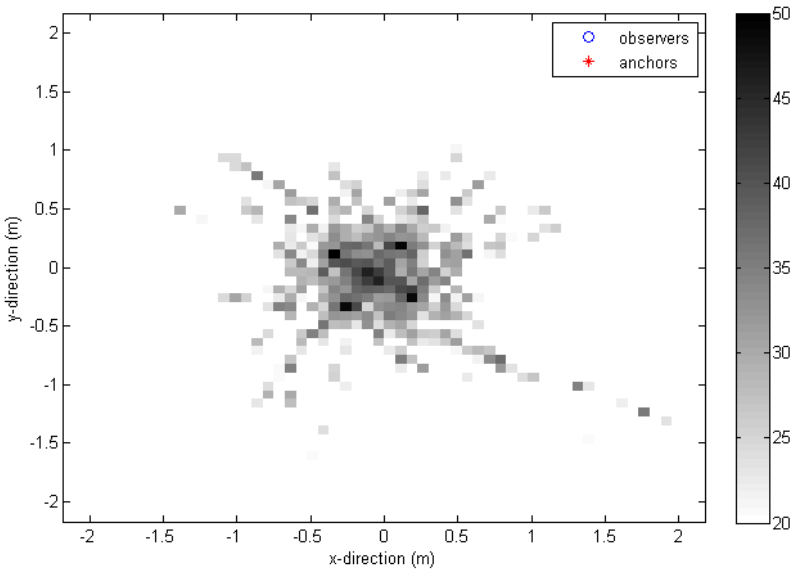

Figure 6.8: 5-Point Moving Target Radar Windowed Image with Modified CBP Based CMTI with SRRS-th

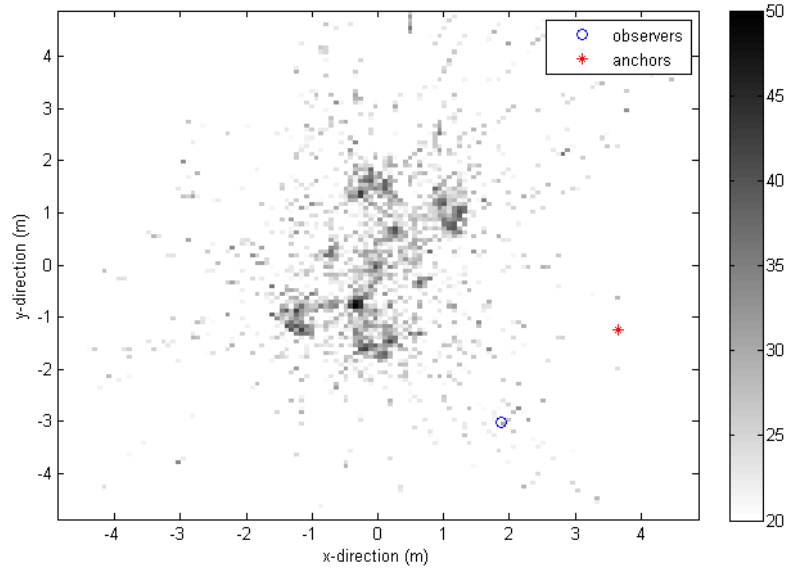

Figure 6.9: 17-Point Moving Target Radar Windowed Image with Modified CBP Based CMTI with SRRS-th

6.2 Average Range Resolution

The first metric by which we evaluate the performance of CMTI is *normalized range resolution error* of bistatic radar structure with respect to the monostatic radar range resolution ΔR_M. According to this metric, first we look at the relation between sensor density and image quality when the number of picture and target velocity are constant. Then secondly, we look at the relation between mobile target velocity and image quality when the number of picture and sensor density are constant. This error is simply a normalized error and can be expressed as,

$$\epsilon_t = \sum_{n=1}^{Nobs} \frac{(\Delta R_B - \Delta R_M)/(\Delta R_M)}{Nobs} \tag{6.1}$$

where $Nobs$ is the number of observations taken by CMTI.

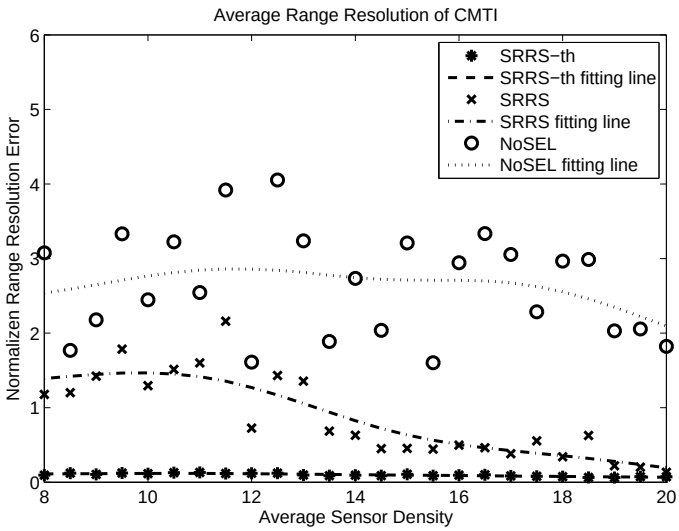

Figure 6.10: Normalized Range Resolution Error ϵ_t vs. Average Sensor Density

As seen in Fig. 6.10, SRRS-th has the minimum range resolution and it has almost the same range resolution as monostatic range resolution. As expected, SRRS-th is decreasing when sensor density is increasing. SRRS reaches to SRRS-th quality performance when sensor field is highly deployed. On the other hand, no selection

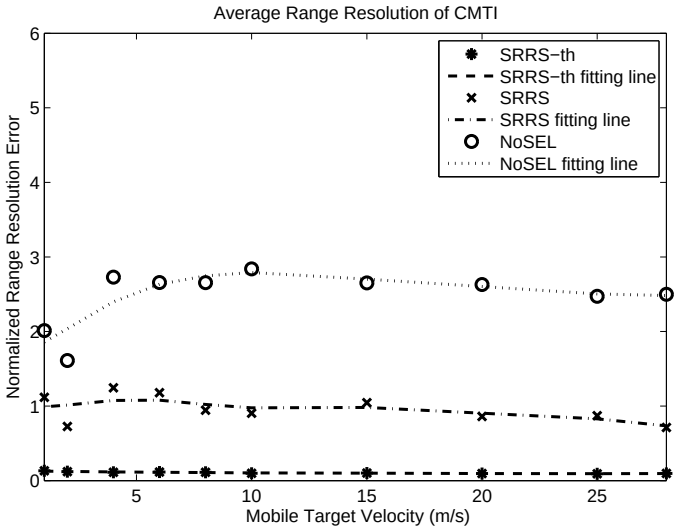

Figure 6.11: Normalized Range Resolution Error ϵ_t vs. Mobile Target Velocity

on range resolution (NoSEL) has nearly 2.5 times worst performance compared to monostatic range resolution.

For varying mobile target velocity case, as in Fig. 6.11, range resolution is not affected for all components. Besides, SRRS-th protects its quality from any change on target velocity.

6.3 Tracking Mean Square Error

The second metric by which we evaluate the performance of CMTI is simply the mean square error in Euclidean 2D space. Specifically, we look at how the computed object locations differ from the actual object locations. In fact, this metric shows only the performance of the target tracking phase. This is the *tracking mean square error* and can be expressed as,

$$\sigma_t^2 = \sum_{i=1}^{N} \frac{(\hat{x}_i - x_i)^2 + (\hat{y}_i - y_i)^2}{N} \tag{6.2}$$

where N is the number of frames, $\hat{x}_i$ and $\hat{y}_i$ are the coordinates of the moving object at frame i determined by CMTI, and x_i and y_i are the actual coordinates of the moving

object at frame *i*.

In CMTI, mobile target is placed to the image plane according to the tracking results. Hence, if there is a considerably high tracking error, target radar image gets blurred.

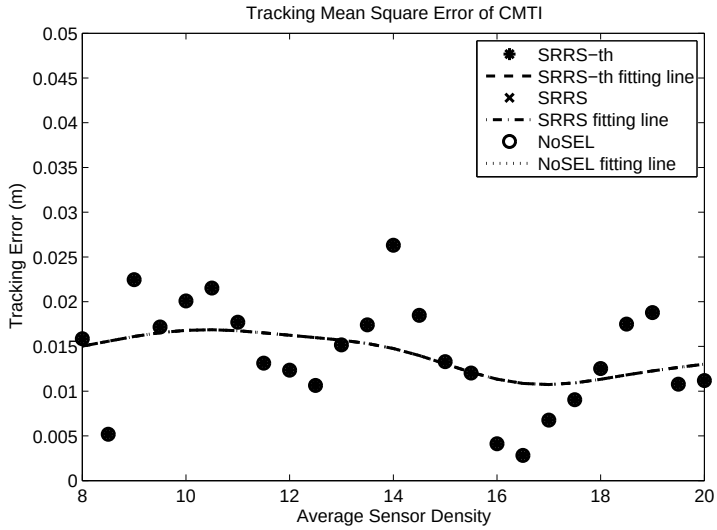

Figure 6.12: Tracking Error σ_t vs. Average Sensor Density

This metric is directly related with the total number of range measurements, which are used in target tracking phase. As in Fig. 6.12, increase in sensor density results a decrease in tracking error as it increases the total number of range measurements to be used in tracking process. Nevertheless, for varying target velocity, as in Fig. 6.13, tracking error remains at the same level. For SRRS-th, SRRS and NoSEL, tracking error remains the same, because *target tracking phase* is completely independent of *ISAC Phase* in CMTI.

6.4 Communication Overhead

The *communication overhead* of the CMTI is also an important performance metric, and is defined as communication overhead incurred by the algorithm or the total data required at sink for imaging process which should be sent by alerted observers in WRSN, and i.e.,

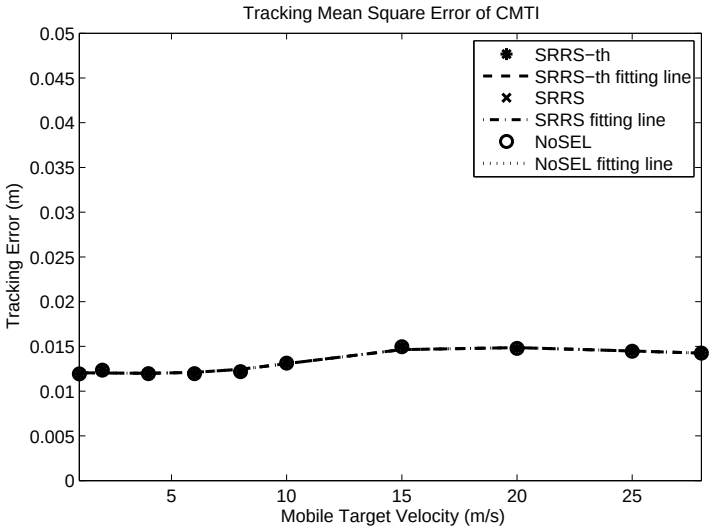

Figure 6.13: Tracking Error σ_t vs. Mobile Target Velocity

$$D_{total} = l_{OBS} Nobs \tag{6.3}$$

where l_{OBS} is the data length of the one observation and $Nobs$ is the number of the observations to be taken in the event field by alerted observers.

As observed from (6.3), the communication overhead is directly related to the number of the observations. In the Fig. 6.14, it is clearly seen that, total data required increases with sensor density. However, the simulations are done for $10s$ and in $10s$ only 10 pictures are taken for imaging. As said before in Section 4.4, in our configuration $ISAMatrix$ perspective size is limited to 360, therefore, only 360 different perspectives can be used for imaging. Then, for lower sensor densities, total data linearly increase until the maximum number of observations is reached.

As seen in Fig. 6.15, for lower velocities, communication overhead is increased until the maximum number of observations is reached. However, communication overhead is not affected by higher mobile target velocity from $5m/s$ to $28m/s$, as the maximum number of observations is reached at this sensor density level. Therefore, it can be deduced that, for higher densities or higher velocities, CMTI

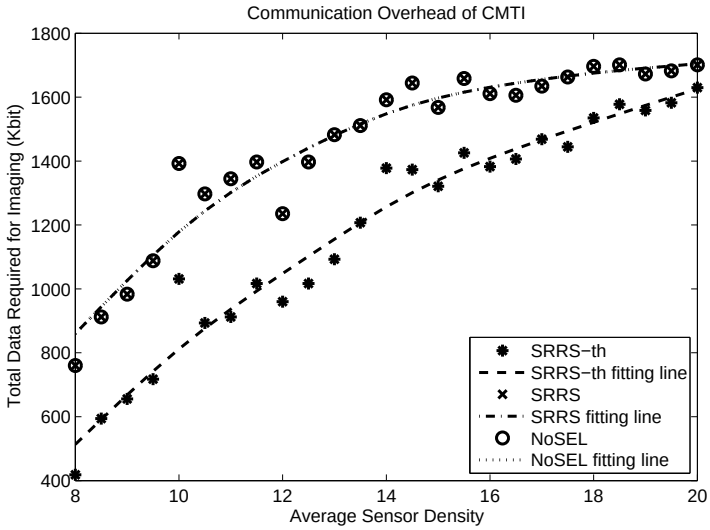

Figure 6.14: Total Data Required for Imaging D_{total} vs. Average Sensor Density

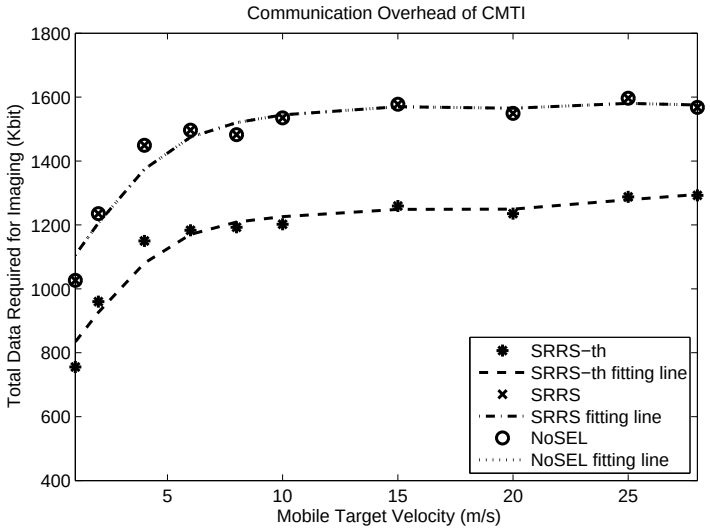

Figure 6.15: Total Data Required for Imaging D_{total} vs. Mobile Target Velocity

is not affected by mobile target velocity.

On the other hand, as observed from (6.3), communication overhead is also directly dependent on data length of the observation. Observation length only changes

when observation window size is changed. However, for different point target models observation window size may change.

6.5 Energy Consumption

Another metric by which the performance of CMTI is evaluated is *energy consumption* during sensor communication in CMTI. Energy consumption generally dominates sensor node lifetime. Energy consumption of the sensor communications in CMTI can be mainly divided into two parts, consumption of observation transport packets (OTP) and range measurement packets (RMP). Here, RMP and OTP are sent with FEC scheme RS(63,5). CMTI control packets (CMP) energy consumption is assumed to be negligible comparing to that of with the other packet types. Energy consumption of the OTPs,

$$E_{OTP} = E_{OTP}^{obs} Nobs \tag{6.4}$$

where E_{OTP}^{obs} is the amount of energy consumed in sending one observation and $Nobs$ is the number of the observations to be taken in the event field by alerted observers. For the RMPs,

$$E_{RMP} = E_{RMP}^{r} N_{anc} N_{obs} F_t T_{total} \tag{6.5}$$

where E_{RMP}^{r} is the energy of sending one range measurement, N_{anc} and N_{obs} is the average number of the alerted anchors and observers in the event field respectively, F_t is the frame frequency and $T_{total} = 10s$ is the total time for $ISAMatrix$ capturing. Then, total energy consumption of CMTI during sensor data communication is given by,

$$E_{CMTI} = E_{OTP} + E_{RMP} \tag{6.6}$$

Accordingly, we look at the relation between this metric and sensor density when mobile target velocity is constant as well as when sensor density is constant.

During the simulations, $T_{total} = 10s$ and $F_t = 100Hz$ are kept constant. As observed from (6.5) and (6.6), total energy consumption is mainly dependent to the

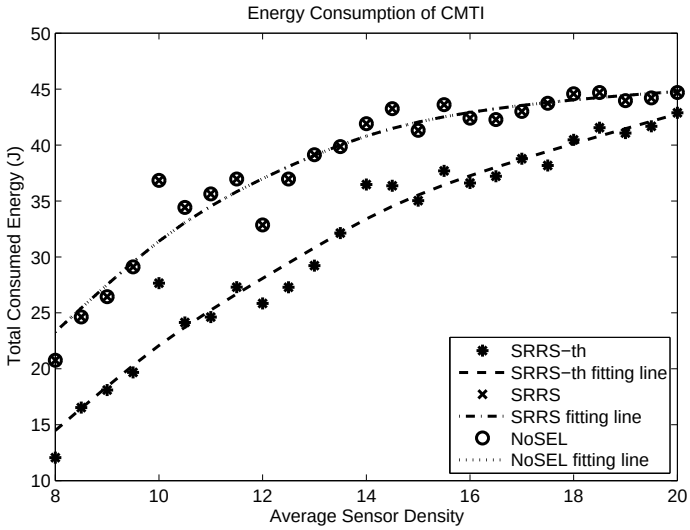

Figure 6.16: Total Consumed Energy E_{CMTI} vs. Average Sensor Density

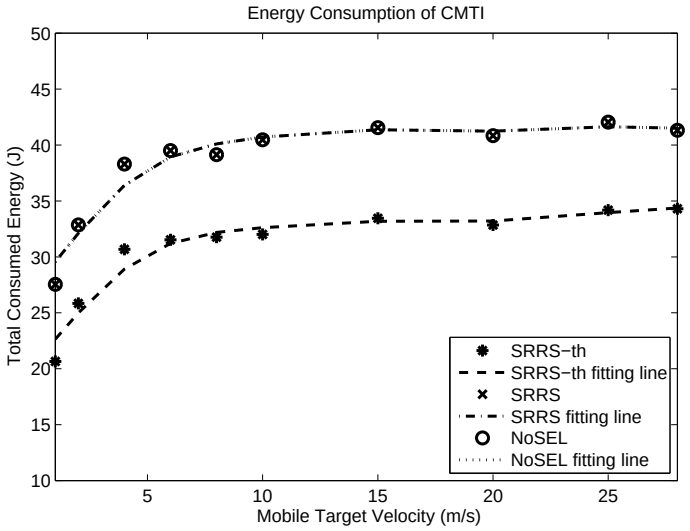

Figure 6.17: Total Consumed Energy E_{CMTI} vs. Mobile Target Velocity

number of observations and to the total number of alerted observers in the field. Besides, E_{OTP} mainly dominates the energy consumption, because amount of observation data is higher than range measurement data. As seen in Fig. 6.16, total

energy consumption of CMTI algorithm increases with the sensor density. Total energy consumption performs the same as total data required for imaging metric, as both are highly dependent on the number of observation taken.

For varying mobile target velocity, as seen in Fig. 6.17, the algorithm performs the same as total data required for imaging metric with the same reason.

CHAPTER 7

CONCLUSION

In wireless sensor networks (WSN), among various target classification methods, imaging of target yields the most valuable information. Imaging of intruder is important for specifying the thread level of the intrusion. In this thesis, an architecture for UWB-WRSN and a new collaborative mobile target imaging (CMTI) algorithm for UWB-WRSN are presented. CMTI algorithm can accurately and efficiently obtain an image of mobile targets based on the collaborative effort of deployed UWB wireless radar sensor nodes.

We presented performance evaluation results of CMTI in terms of average range resolution, tracking error, total data required for imaging and energy consumption. Therefore, smallest range resolution selection with threshold (SRRS-th) component is very suitable for a WRSN structure, because SRRS-th has better performance, according to all metrics in the Chapter 6.

We presented a mobile target imaging algorithm with using UWB radar sensors in the field. However, this algorithm can be adapted for wireless acoustic sensor networks either for the use in land or underwater environment as a future work. Especially, tracking phase of CMTI must be modified according to the acoustic environmental parameters.

As mentioned in Section 2.2.2, sensor node's transceivers can be configured with UWB technology for high data rate, low-cost and low-power. In our proposed WRSN structure, radar sensor nodes can be equipped with UWB transceiver. In this

way, lifetime of the radar sensor nodes can be extended. Therefore, as a future work, the effect of UWB wireless communication on RIOT phase in CMTI can evaluated.

In CMTI, all radar sensor nodes can send their observation packets with other than RS codes, like convolutional, Luby Transform (LT) and Raptor codes. LT and Raptor codes have really important advantages on decoding speed and decoding complexity for resource constraint WSN. As a future work, the effect of these codes can be evaluated, also latency of these codes can be investigated for the performance of real-time tracking in WRSN.

Performance evaluations reveal that CMTI algorithm obtains high quality radar image of mobile targets in WRSN with very low communication overhead, using observation windowing, reliability and energy expenditure, using RS(63,53,5) codes. Experiment results show that its performance is not affected by the shape and velocity of mobile targets and the channel conditions.

REFERENCES

[1] Federal Communications Commission, "Revision of Part 15 of the Commissions Rules Regarding UWB Transmission Systems," First Report, *FCC* 02-48, April 2002.

[2] "Wireless Communication Standard, IEEE 802.15.4a," http://www.ieee802.org/15/pub/TG4a.html.

[3] T. W. Barrett, "History of Ultra-Wideband (UWB) Radar & Communications: Pioneers and Innovators," in Progress In Electromagnetics Symposium 2000, *PIERS2000*, Cambridge, MA, July 2000.

[4] I. Immoreev, "Ten Questions on UWB," *IEEE AES Systems Magazine*, November 2003.

[5] M. Shen, T. Koivisto, T Peltonen, L. Zheng, E. Tjukanoff, H. Tenhunen, "UWB Radio Module Design for Wireless Sensor Networks," *23rd NORCHIP Conference, 2005*, pp. 184-187, 21-22 November 2005.

[6] S. Colson, H. Hoff, "Ultra-Wideband Technology for Defence Applications", *IEEE International Conference on Ultra-Wideband, ICU, 2005*, pp. 615-620, 5-8 September 2005.

[7] J. D. Taylor, "Ultra-WideBand Radar Technology," *CRC Press LLC*, 2001.

[8] M. I. Skolnik, "Introduction to Radar Systems," *McGraw-Hill Higher Education*, Third Edition, 2001.

[9] D.R. Wehner, "High Resolution Radar," *Artech House, Inc.*, ISBN 0-89006-194-7, 1987.

[10] R.J. Sullivan, "Radar Foundations for Imaging and Advance Concepts," *Scitech Publishing Inc.*, ISBN 1-891121-22-7, 2004.

[11] N.J. Willis, "Bistatic Radar," *Scitech Publishing Inc.*, 2005.

[12] T.S. Rappaport, "Wireless Communications: Principles and Practice," *Prentice-Hall*, Second Edition, 2001.

[13] R.S. Thoma, O. Hirsch, J. Sachs, R. Zetik, "UWB Sensor Networks for Position Location and Imaging of objects and Environments," *EUCAP2007*, November 2007.

[14] E. Paolini, A. Giorgetti, M. Chiani, R. Minutolo, M. Montanari, "Localization Capability of Cooperative Anti-Intruder Radar Systems," *EURASIP'08*, Volume 2008, Article ID 726854, March 2008.

[15] P.K. Dutta, A.K. Arora, and S.B. Bibyk, "Towards Radar-Enabled Sensor Networks," *IPSN'06*, April 2006.

[16] S. Azevedo, T.E. McEwan, "Micropower Impulse Radar," *Science & Technology Review*, January/February, 2006.

[17] J. Sachs, M. Kmec, R. Herrmann, P. Peyerl, P. Rauschenbach, "An Ultra-Wideband Pseudo-Noise Radar Family integrated in SiGe:C," *Proceedings of the International Radar Symposium IRS 2006*, May 2006.

[18] J. Sachs, P. Peyerl, R. Zetik, S. Crabbe, "M-Sequence Ultra-Wideband-Radar: State of Development and Applications," *IEEE Radar 2003*, Adelaide, Australia, 3-5 September 2003.

[19] S. Foo, S. Kashyap, "Cross-correlated back projection for UWB radar imaging," *Antennas and Propagation Society International Symposium, 2004*, Volume 2, pp. 1275-1278, June 2004.

[20] R. Zetik, J. Sachs and R. Thoma, "Modified Cross-Correlation Back Projection for UWB Imaging: Numerical Examples," *Ultra-Wideband, 2005. ICU 2005. 2005 IEEE International Conference*, pp. 5, 5-8 September 2005.

[21] J. Jerabek, D. Dvorak, J. Mrkvica, R. Sikl, "Moving Target UWB Radar Demonstration using Real-Time Sampling," *Radioelektronika, 2007. 17th International Conference*, pp. 1-4, 24-25 April 2007.

[22] C. Chang, A. Sahai, "Object Tracking in a 2D UWB Sensor Network," *IEEE Proceedings of the 38th Asilomar Conference on Signals, Systems and Computers*, vol. 1, pp. 1252-1256, Pacific Grove, CA, USA, November 2004.

[23] M. Tobias, A.D. Lanterman "Probability Hypothesis Density-Based Multitarget Tracking With Bistatic Range and Doppler Observations," in *Radar, Sonar and Navigation, IEE. Proceedings*, vol. 152, issue 3, 3 June 2005, pp. 195-205.

[24] N.J. Mohamed, "Target Signature Using Nonsinusoidal Radar Signals," *IEEE Transactions on Electromagnetic Compatibility*, vol. 35, no. 11, pp. 457-465, November 1993.

[25] M. Picardi, “Background Subtraction Techniques: A Review,” *In Proceedings of International Conference on Systems, Man and Cybernetics*, The Hague, The Netherlands, October 2004.

[26] R. Zetik, S. Crabbe, J. Krajnak, P. Peyerl, J. Sachs, R. Thoma, “Detection and Localization of Persons Behind Obstacles Using M-sequence Through-the-wall Radar,” *In Proceedings of SPIE, Sensors, and Command, Control, Communications, and Intelligence Technologies for Homeland Security and Homeland Defense*, vol. 6201, May 2006.

[27] H. Sheng, P. Orlik, A.M. Haimovich, L.J. Cimini, and J. Zhang, “On the Spectral and Power Requirements for Ultrawideband Transmission,” *in Proc. IEEE Int. Conf. on Communications,*, vol. 1, Anchorage, USA, May 2003, pp. 738-742.

[28] C. Wang, M. Daneshmand, B. Li, K. Sohraby, “A Survey of Transport Protocols for Wireless Sensor Networks,” *IEEE Network Magazine Special Issue on Wireless Sensor Networking*, 20(3):34-40, 2006.

[29] M. Svecova, D. Kocur, R. Zetik, “Object Localization Using Round Trip Propagation Time Measurements,” *IEEE Radioelektronika 2008*, 24-25 April 2008, pp. 1-4.

[30] N. Patwari, J.N. Ash, S. Kyperountas, A.O. Hero III, R.L. Moses, and N.S. Correal, “Locating the Nodes - Cooperative localization in wireless sensor networks,” *IEEE Signal Processing Magazine*, July 2005.

[31] F. Chiti, R. Fantacci, S. Menci, A. Zappoli, “Cooperative Localization Protocols for Wireless Sensor Networks,” *IEEE GLOBECOM 2007*, 2007.

[32] D. Wei, H.A. Chan, “A Survey on Cluster Schemes in Ad Hoc Wireless Networks,” *IEE Mobility Conference*, GuangZhou, 2005.

[33] S. Kim, R. Fonseca, D. Culler, “Reliable Transfer on Wireless Sensor Networks,” *Sensors and Ad Hoc Communications and Networks, IEEE SECON 2004*, pp. 449-459, 4-7 October 2004.

[34] H. Wen, C. Lin, F. Ren, Y. Yue, X. Huang, “Retransmission or Redundancy: Transmission Reliability in Wireless Sensor Networks,” *IEEE MASS 2007*, 8-11 October 2007, pp. 1-7.

[35] Z. Tian, D. Yuan, Q. Liang, “Energy Efficiency Analysis of Error Control Schemes in Wireless Sensor Networks,” *IEEE International Wireless Communications and Mobile Computing Conference, 2008 (IWCMC’08)*, 6-8 August 2008, pp. 401-405.

[36] Z.H. Kashani, Z. Shiva, “BCH Coding and Multi-hop Communication in Wireless Sensor Networks,” *International Conference on Embedded And Ubiquitous Computing (IFIP’06)*, Seul, Korea, 11-13 April 2006.

[37] M.C. Vuran, I.F. Akyildiz, “Cross-Layer Analysis of Error Control in Wireless Sensor Networks,” *3rd Annual IEEE Communications Society on Sensor and Ad Hoc Communications and Networks (SECON ’06)*, Reston VA, USA, 25-28 September 2006.

[38] Y. Sankarasubramaniam, I.F. Akyildiz, S.W. McLaughlin, “Energy Efficiency Based Packet Size Optimization in Wireless Sensor Networks,” *IEEE International Workshop on Sensor Network Protocols and Applications*, 2003, pp. 1-8.

[39] Z.H. Kashani, M. Shiva, “Channel Coding in Multi-hop Wireless Sensor Networks,” *IEEE 6th International Conference on ITS Telecommunications Proceedings*, 2006.

[40] F. Stann, J. Heidemann, “RMST: Reliable Data Transport in Sensor Networks,” *IEEE SNPA 2003*, Anchorage, Alaska, USA, 11 May 2003.

[41] Y. Sankarasubramaniam, O.B. Akan, I.F. Akyildiz, “ESRT: Event-to-Sink Reliable Transport in Wireless Sensor Networks,” *IEEE MobiHoc’03*, Annapolis, Maryland, USA, June 1-3, 2003.

[42] H. Zang, A. Arora, Y. Choi, M.G. Gouda, “Reliable Bursty Convergecast in Wireless Sensor Networks,” *IEEE MobiHoc’05*, Urbana-Champain, Illinois, USA, May 25-28, 2005.

[43] K. Sohrabi, B. Manriquez and G. Pottie, “Near-Ground Wideband Cahnnel Measurements,” *Proc. IEEE VTC’99*, New York, USA, 1999.

[44] IEEE Standard for Information Technology - Telecommunications and information exchange between systems - Local and metropolitan area networks - specific requirement Part 15.4: Wireless Medium Access Control (MAC) and Physical Layer (PHY) Specifications for Low-Rate Wireless Personal Area Networks (WPANs), 2006.

[45] A. Sinha, A.P. Chandrakasan, ”JouleTrack: a web based tool for software energy profiling”, *In Proceedings of the 38th Conference on Design Automation*, Las Vegas, Nevada, United States, June 2001, pp. 220-225.

[46] “DIGITAL Semiconductor SA-1100 Microprocessor DataSheet”.

[47] “RF Monolithics Inc. 916.50 MHz Hybrid Transceiver TR1000,” http://www.RFM.com.

[48] “ASH Transceiver Designer Guide,” http://www.rfm.com/products/tr_des24.pdf.

APPENDIX A

ENERGY EFFICIENCY OF RELIABLE IMAGING OBSERVATION TRANSPORT

In order to select a reliable and energy efficient imaging observation transportation method, we explore two reliable communication methods, i.e., retransmission (ARQ) and FEC error control schemes on link layer protocols, in terms of an optimization metric of energy efficiency which is proposed in [38].

A suitable metric that captures the energy and reliability constraints is the energy efficiency η, which is defined as [38],

$$\eta = \eta_e r = \frac{E_{eff}}{E_{total}}(1 - PER) \tag{A.1}$$

where $\eta_e = E_{eff}/E_{total}$ is the energy throughput and $r = (1 - PER)$ is the packet acceptance rate and PER is the packer error rate [38].

We focus on link layer protocols in sensor networks, and hop-by-hop error control strategy is discussed. For this analysis, we assume WRSN nodes the $\mu AMPS$ sensor node with $Strong\ ARM$ 1100 [46] processor and $RFM - TR1000$ [47] radio module as in [36].

For RFM-TR1000 transceiver, the average received bit energy per noise ratio γ is calculated as in [38] and [48] with average output power $P_o = -9dBm$, receiver noise figure $F_n = 7.5dB$ and $L_I = 6dB$ implementation loss,

$$\gamma = 77 - 10\beta log(d) \tag{A.2}$$

where β is the path loss exponent and d is the transmitter to receiver distance. For flat Rayleigh fading β is selected as 3.5.

In the analysis for ARQ, stop-and-wait ARQ scheme with packet size $800bits$. For FEC, binary BCH codes are used with block lengths of 31,127,511,2047, and RS codes are used with block lengths 31,63,127,255 with error correcting capabilities $t = 1, 3, 5$ to send different windowed observation sizes as $3200bits$, maximum $16000bits$.

Then, optimization metric for energy efficiency of CMTI is,

$$\eta_{CMTI} = \frac{E_{eff}}{E_{total}} r_{obs} \tag{A.3}$$

where $r_{obs} = (1 - OER)$ is the observation acceptance rate and OER is the observation error rate.

Then, first we calculate energy throughput for ARQ and FEC to find energy efficiency. Energy consumption of a sensor node for communication over one hop for stop-and-wait ARQ scheme with DATA+ACK handshake can be expressed by [35],

$$E_{ARQ} = E_{ARQ}^{TX} + E_{ARQ}^{RX} \tag{A.4}$$

where $E_{\cdot}^{TX}$ is the energy consumed by sensor node when transmitting a packet and $E_{\cdot}^{RX}$ is the energy consumed by sensor node when receiving a packet [36], [38].

$$E_{ARQ}^{TX} = (E_t l_{DATA}) + (E_r l_{ACK}) + (E_{tst} + E_{rst}) \tag{A.5}$$

$$E_{ARQ}^{RX} = (E_r l_{DATA}) + (E_t l_{ACK}) + (E_{tst} + E_{rst}) \tag{A.6}$$

where E_t, E_r are the energy consumption of transmitter and receiver per bit, E_{tst}, E_{rst} are the start-up energy consumption of transmitter and receiver, l_{DATA}, l_{ACK} are the bit length of the data and acknowledgment, respectively.

For RFM-TR1000 radio modules, which use non-coherent detection of FSK modulation scheme, bit error rate of NCFSK on a Rayleigh frequency non-selective fading channel is given by [12],

$$P_b = \frac{1}{2 + \gamma} \tag{A.7}$$

Figure A.1: MAC Frame Format of DATA in 802.15.4 [44]

where γ is the averaged received bit energy to noise ratio. The PER of ARQ scheme,

$$PER_{ARQ} = 1 - (1 - p_b)^{l_{DATA}+l_{ACK}} \tag{A.8}$$

where $l_{DATA} = \alpha + l_{PAYLOAD}$ is the packet size of the observation, $\alpha = l_{MHR} + l_{FCS}$, l_{MHR} is the length of header (MHR), l_{FCS} is the frame check sequence (FCS) as shown in Fig. A.1 and $l_{PAYLOAD} = l_{OTP} = l_{HDR} + l_{OBS}$ is the length of the Observation Transport Packet (OTP) of CMTI, l_{OBS} is the data length of the one observation and l_{HDR} is the data length of the observation header, as shown in Fig.4.3.

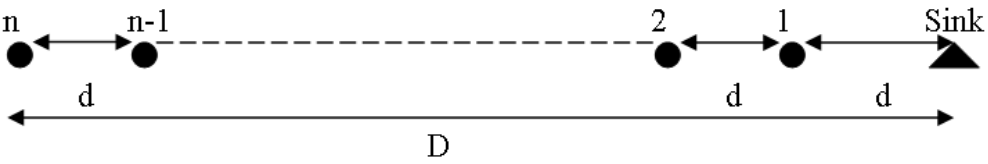

Figure A.2: Linear Packet Forwarding Model

Generally, network topology and location of nodes are randomly selected for WSN, however, in our analysis a linear model is used for multi-hop communication as in [36]. One such linear model of packet forwarding from end-node to sink is illustrated in Fig. A.2.

For stop-and-wait ARQ scheme, energy consumption of one observation data for communication over h hop with r retransmission attempts,

$$E_{ARQ}^{(r,h)} = \left(h\left(E_{ARQ}^{TX}\right) + (h-1)\left(E_{ARQ}^{RX}\right)\right)\left(\frac{\left(1 - PER_{ARQ}^{r}\right)}{(1 - PER_{ARQ})}\right) \tag{A.9}$$

$$E_{ARQ}^{CMTI} = E_{ARQ}^{(r,h)}(\lceil \frac{l_{OBS}}{k_{ARQ}} \rceil) \tag{A.10}$$

where $\lceil . \rceil$ is the ceiling function and k_{ARQ} is the packet length of ARQ scheme.

Energy efficiency of CMTI with ARQ scheme with h hops and r maximum retransmission can be calculated by,

$$\eta_{CMTI} = \frac{E_{ARQ}^{effi}}{E_{ARQ}^{CMTI}} r_{ARQ}^{obs} \tag{A.11}$$

where

$$r_{ARQ}^{obs} = 1 - OER = 1 - \left(1 - \left(1 - \left(1 - PER_{ARQ}^{r}\right)^{h}\right)\right)^{\lceil \frac{l_{OBS}}{k_{ARQ}} \rceil} \tag{A.12}$$

After ARQ scheme, energy consumption of a sensor node for communication over one hop for FEC scheme with BCH(n,k,t) and RS(n,k,t),

$$E_{FEC} = E_{FEC}^{TX} + E_{FEC}^{RX} + E_{dec} \tag{A.13}$$

where encoding energy consumed by a sensor node is considered to be negligible small [36] and E_{dec} is the decoding energy. For some binary BCH(n,k,t) and RS(n,k,t) codes, decoding energies are stated in [36] and [39] with *Strong ARM* 1100 microprocessor from JouleTrack (a web based tool for software energy profiling) [45]. For BCH and RS codes considered here, we assume perfect interleaving at the transceiver and coded block error rate is defined as [37],

$$BLER(n,k,t) = 1 - \sum_{i=0}^{t} \binom{n}{i} p_{FEC}^{i} (1 - p_{FEC})^{n-i} \tag{A.14}$$

where $p_{FEC} = P_b$ is bit error probability for binary BCH codes and $p_{FEC} = P_s = 1 - (1 - P_b)^s$ is symbol error rate for RS(n,k,t) codes, where $s = log_2(n + 1)$ is the symbol length. Since a windowed observation of CMTI is generally larger than block length n. Then, the observation error rate (OER) for FEC is given by [37],

$$OER\,(l_{OBS}, n, k, t) = 1 - (1 - BLER\,(n,k,t))^{\lceil \frac{l_{OBS}}{k} \rceil} \tag{A.15}$$

where $\lceil \frac{l_{OBS}}{k} \rceil$ is the number of blocks required to send l_{OBS} bits.

For FEC scheme with BCH(n,k,t) and RS(n,k,t), energy consumption of one observation data for communication over h hop,

$$E_{FEC}^{h} = \left(h\left(E_{FEC}^{TX}\right) + (h-1)\left(E_{FEC}^{RX} + E_{dec}\,(n,t)\right)\right) \tag{A.16}$$

$$E_{FEC}^{CMTI} = E_{FEC}^{h}\left(\lceil\frac{l_{OBS}}{k}\rceil\right) \tag{A.17}$$

Energy efficiency of CMTI with FEC scheme with h hops can be calculated by,

$$\eta = \frac{E_{FEC}^{effi}}{E_{FEC}^{CMTI}} r_{FEC}^{obs} \tag{A.18}$$

where

$$r_{FEC}^{obs} = 1 - OER = 1 - (1 - (1 - (1 - BLER)^{h}))^{\lceil\frac{l_{OBS}}{k_{FEC}}\rceil} \tag{A.19}$$

and $k_{FEC} = k_{BCH}$ is the data length for BCH(n,k,t) codes or $k_{FEC} = k_{RS}(log_2(n+1))$ is the data length for RS(n,k,t) codes.

For sensor node used in WRSN as $\mu AMPS$ with RFM-TR1000 radio module, according to the parameters in the Table A.1, energy efficiencies of CMTI for nominal (3200$bits$) and maximum (16000$bits$) observation data sizes are calculated over multi-hop communication.

For communicating one hop neighbor node with observation size 3200$bits$, Fig. A.3 illustrates energy efficiency of CMTI with ARQ and different BCH codes and Fig. A.4 illustrates energy efficiency of CMTI with ARQ and different RS codes. It is clearly seen that RS codes totally have higher efficiency than BCH codes. For a typical neighbor distances 20-30 meters in WSN [43], the raw BER ranges between 7×10^{-4} and 3×10^{-3} for NCFSK modulated data under flat fading [38]. It is seen in the Fig. A.4 that for these BER values, RS(63,3) and RS(63,5) codes seem to perform with higher energy efficiency for CMTI.

For communicating one hop neighbor node with maximum observation size 16000$bits$, Fig. A.5 and Fig. A.6 illustrate energy efficiency of CMTI with ARQ and different BCH codes and different RS codes, respectively. As for 3200$bits$, it is clearly seen that RS codes yield higher efficiency than BCH codes. As in Fig. A.6,

Table A.1: Radio Parameters

Parameters		
Symbol	***Definition***	***Quantity***
P_t	transmit power	$-9dBm$
F_n	receiver noise figure	$7.5dB$
L_I	implementation loss	$6dB$
α	sum of MHR and FCS size	$11byte$
l_{ACK}	ACK size	$7byte$
l_{HDR}	OTP header size	$9byte$
E_t	energy consumed in TX circuitry	$1.066\mu J/bit$
E_r	energy consumed in RX circuitry	$0.533\mu J/bit$
R_{radio}	raw data rate	$19.2kbits/s$

for typical BER values, RS(63,5) codes seem to be more energy efficient for CMTI at $16000bits$. On the other hand, for very low BER values as 10^{-5}, ARQ schemes seem to be more energy efficient for CMTI.

For more real case as multi-hop with end-node to sink distance at $200m$, Fig. A.7 and A.8 illustrate energy efficiency of CMTI with ARQ and different RS codes. For typical neighbor distances 20-30 meters in WSN [43], typical hop count varies from 7 to 10 hops when end-node to sink distance is $200m$. It is seen in the Fig. A.7 and A.8 that at these hop counts RS(63,5) code seems to be more energy efficient for CMTI at sink distance $200m$. On the other hand, for high hop count numbers ARQ schemes becomes more energy efficient than FEC schemes for CMTI. However, it is obvious that, increase on hop count causes increase on latency of network.

In CMTI, for reliable imaging observation transport over multi-hop, FEC scheme with RS codes is more energy efficient and RS(63,53,5) scheme is suggested from the analysis.

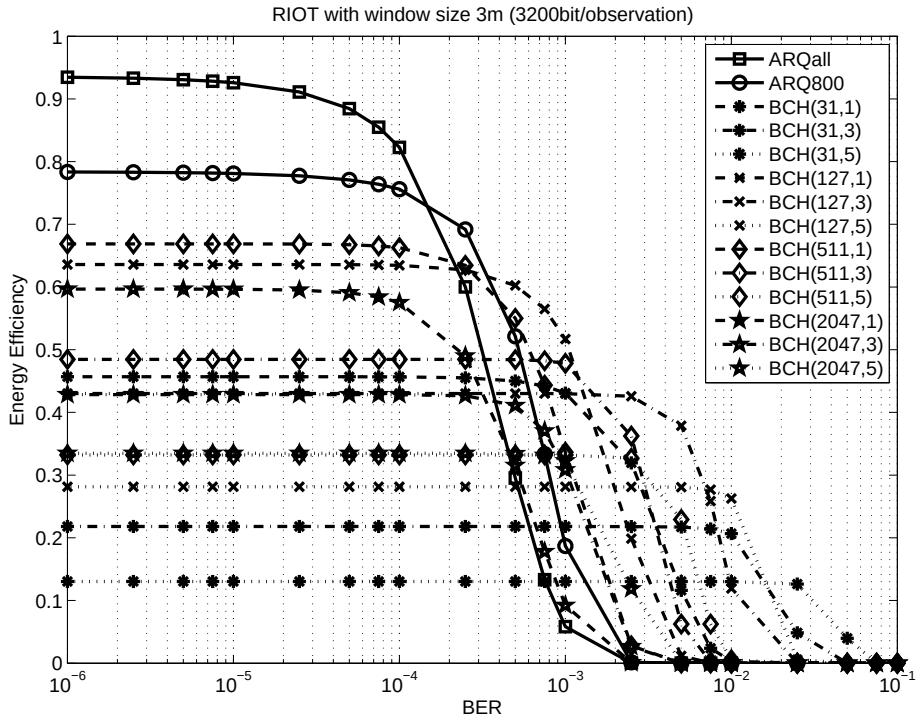

Figure A.3: Channel Bit Error Rate vs. Energy Efficiency of RIOT for ARQ & FEC Schemes with Different BCH Codes for Reliable Imaging Observation Transport When Window Size is 3200$bits$

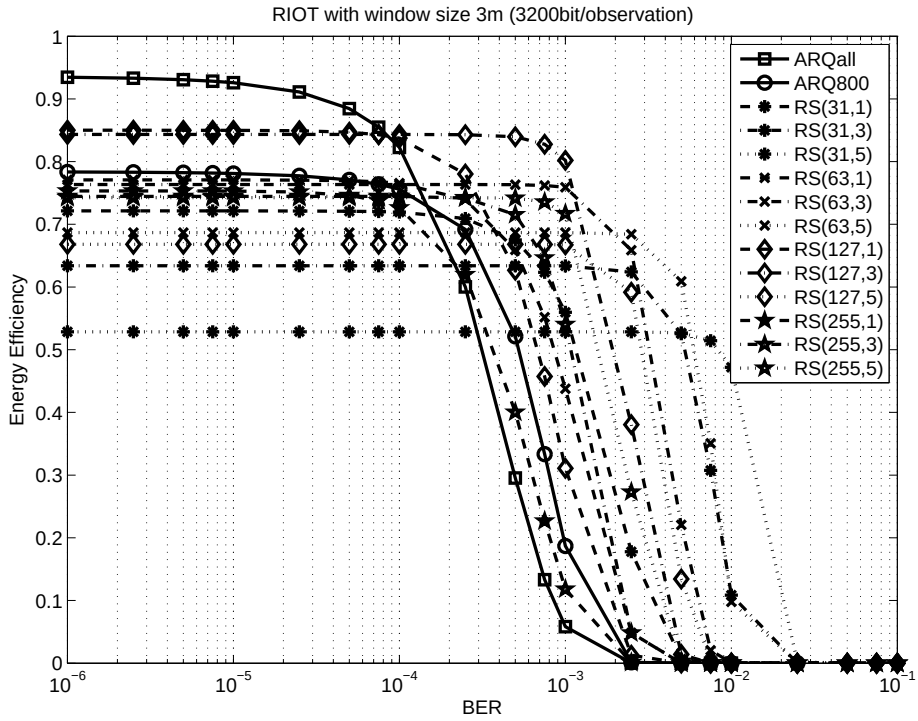

Figure A.4: Channel Bit Error Rate vs. Energy Efficiency of RIOT for ARQ & FEC Schemes with Different RS Codes for Reliable Imaging Observation Transport When Window Size is 3200$bits$

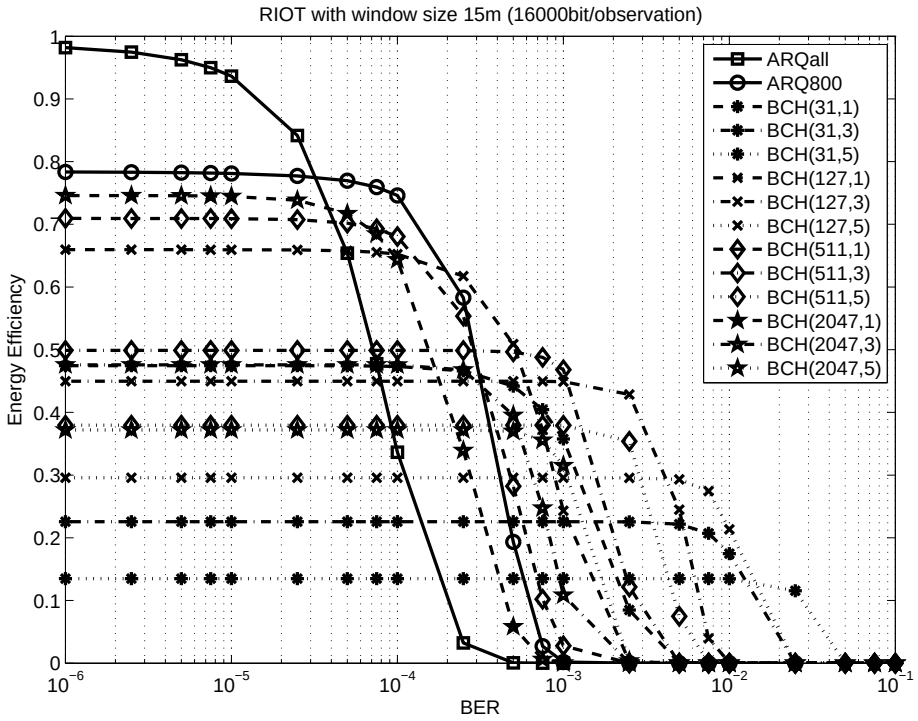

Figure A.5: Channel Bit Error Rate vs. Energy Efficiency of RIOT for ARQ & FEC Schemes with Different BCH Codes for Reliable Imaging Observation Transport When Window Size is 16000$bits$

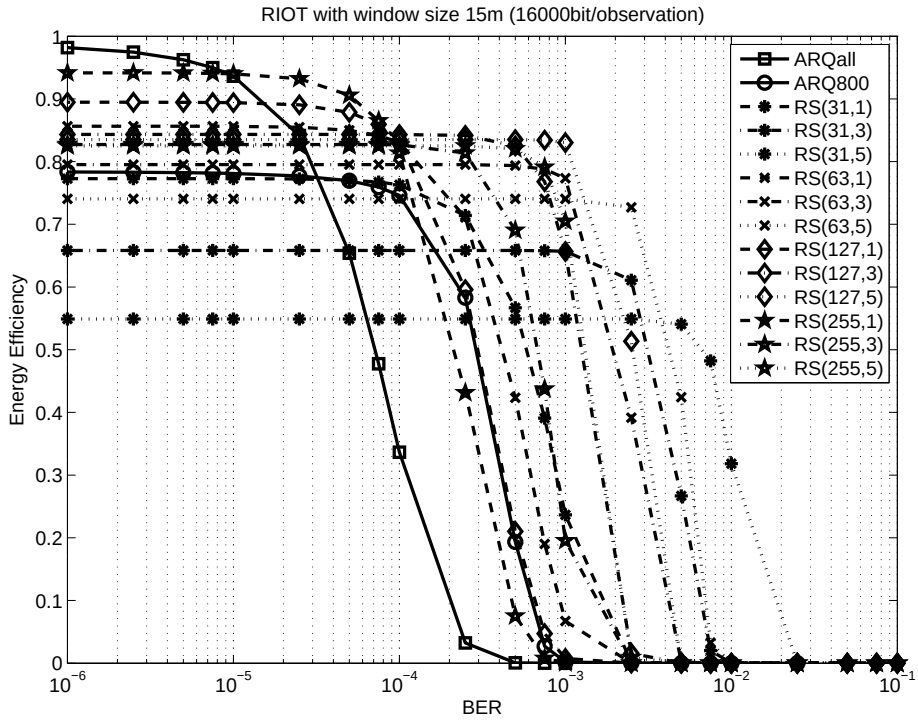

Figure A.6: Channel Bit Error Rate vs. Energy Efficiency of RIOT for ARQ & FEC Schemes with Different RS Codes for Reliable Imaging Observation Transport When Window Size is 16000$bits$

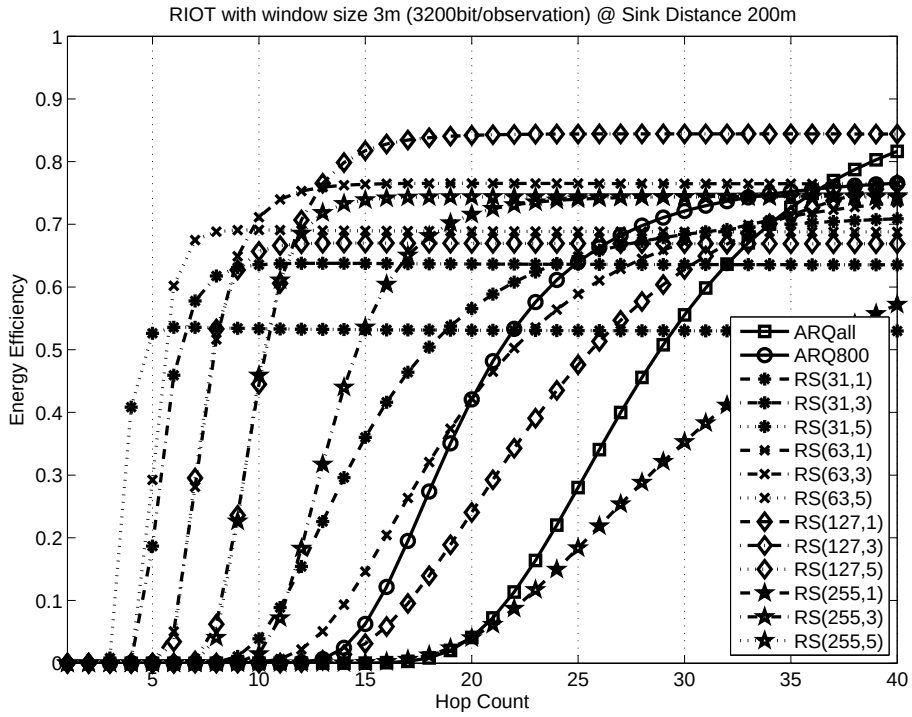

Figure A.7: Hop Count vs. Energy Efficiency of RIOT for ARQ & FEC Schemes with Different RS Codes for Reliable Imaging Observation Transport When Window Size is 3200$bits$ and Sink Distance is 200m

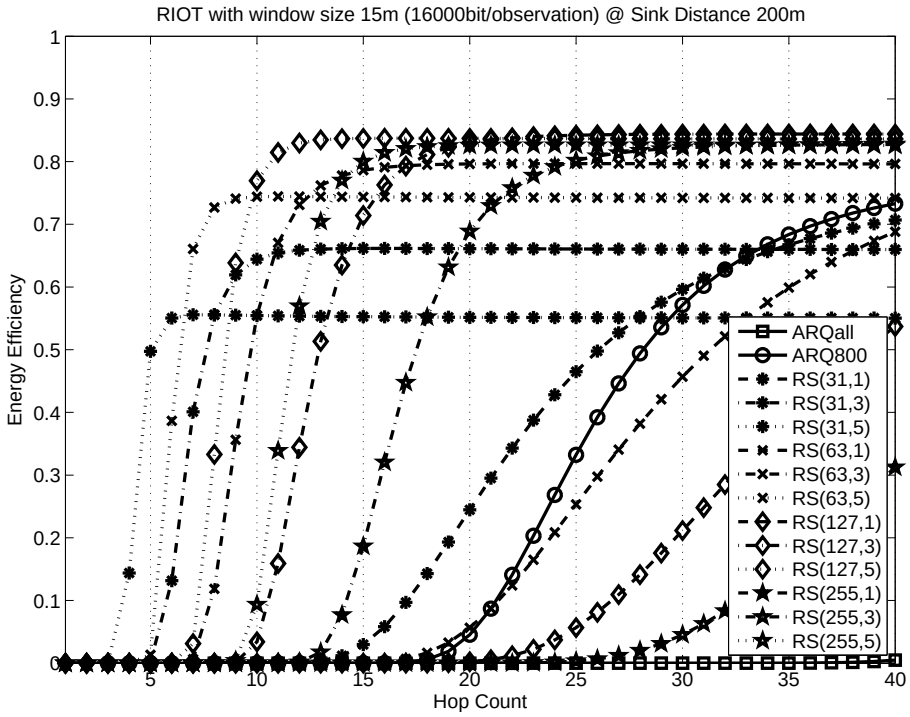

Figure A.8: Hop Count vs. Energy Efficiency of RIOT for ARQ & FEC Schemes with Different RS Codes for Reliable Imaging Observation Transport When Window Size is 16000$bits$ and Sink Distance is 200m